Suomi National Polar Partnership Mission

Algorithm Theoretical Basis Document

NASA L1b: Advanced Technology Microwave Sounder

Version 1

July 2014

Prepared by:

B. H. Lambrigtsen, JPL

Version History

Version 0.1	April 2005	Initial draft, based on SDR version 2.2
Version 0.2	June 2014	Revised based on JPSS versions
Version 0.3	June 2014	Revised based on Aqua/MW L1b version 2.1
Version 1	July 2014	Peer review version

Table of Contents

Illustrations

Tables

Acronyms

ADC	Analog-to-digital converter
AIRS	Atmospheric Infrared Sounder
AMSU	Advanced Microwave Sounding Unit
ARM	Atmospheric Radiation Measurement program
ATBD	Algorithm Theoretical Basis Document
ATMS	Advanced Technology Microwave Sounder
ATOVS	Advanced TOVS
CDR	Climate Data Record
CrIMSS	Cross-track Infrared and Microwave Sounding Suite
CrIS	Cross-track Infrared Sounder
DN	Data number
EDR	Environmental Data Record
EDU	Engineering Development Unit
EOS	Earth Observing System
EOSDIS	EOS Data and Information System
EU	Engineering unit
FRD	Functional Requirements Document
GSFC	Goddard Space Flight Center
HAMSR	High Altitude MMIC Sounding Radiometer
HIRS	High resolution Infrared Radiation Sounder
IF	Intermediate frequency
IMAS	Integrated Multispectral Atmospheric Sounder
IPO	Integrated Program Office
IORD	Integrated Operational Requirements Document
IR	Infrared
JPL	Jet Propulsion Laboratory
JPSS	Joint Polar Satellite System
LO	Local oscillator
MHS	Microwave Humidity Sounder
MIT	Massachusetts Institute of Technology
MMIC	Monolithic Microwave Integrated Circuit
MSU	Microwave Sounding Unit
MUX	Multiplexer
MW	Microwave
NASA	National Aeronautic and Space Administration
NEDT	Noise-equivalent delta-T
NGES	Northrop Grumman Electronic Systems
NGST	Northrop Grumman Space Technologies
NOAA	National Oceanic and Atmospheric Administration
NPOESS	National Polar-orbiting Operational Environmental Satellite System
NPP	National Polar Partenrship
	NPOESS Preparatory Project
NWP	Numerical Weather Prediction
NWS	National Weather Service
ORD	Operational Requirements Document

PLLO	**P**hase **l**ocked **l**ocal **o**scillator
POES	**P**olar-orbiting **O**perational **E**nvironmental **S**atellite
POS	**P**erformance and **O**perations **S**pecification
PRT	**P**latinum **r**esistance **t**hermometer
QA	**Q**uality **a**ssessment
QC	**Q**uality **c**ontrol
RDR	**R**aw **D**ata **R**ecord
RF	**R**adio **f**requency
SDR	**S**ensor **D**ata **R**ecord
SNPP	**S**uomi **N**ational **P**olar **P**artnership
SSM/IS	**S**pecial **S**ensor — Microwave **I**mager/**S**ounder
SSM/T	**S**pecial **S**ensor — **M**icrowave **T**emperature sounder
TIROS	**T**elevision **I**nfrared **O**bservation **S**atellite
TOVS	**T**IROS **O**perational **V**ertical **S**ounder
WMO	**W**orld **M**eteorological **O**rganization
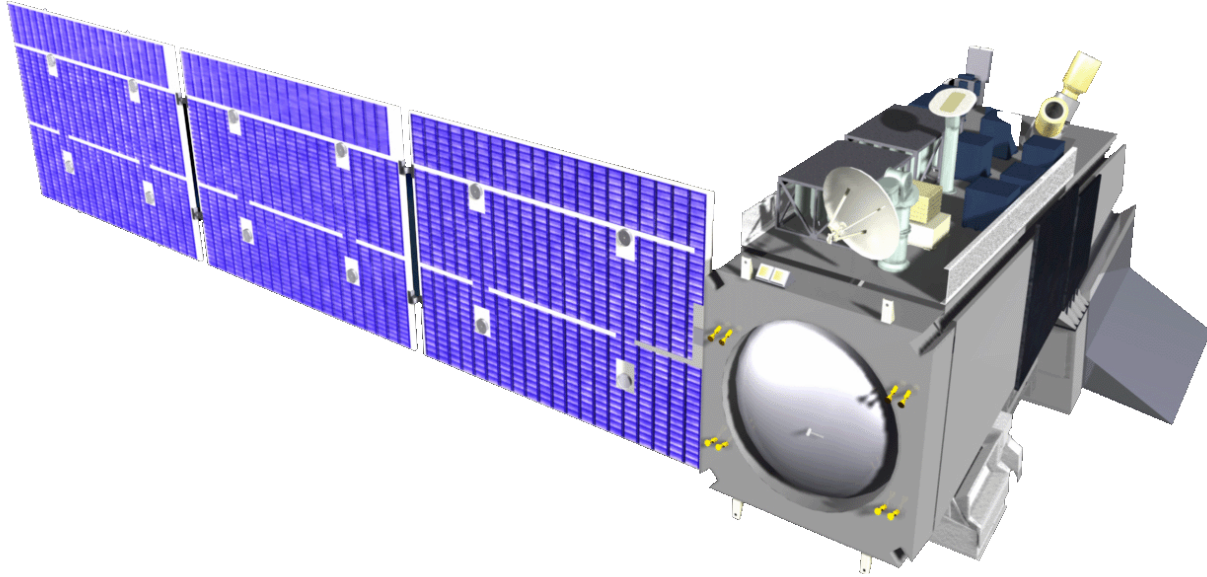
NPP spacecraft

Introduction

The Level 1b ATBD describes the theoretical basis and, to some extent, the form of the algorithms used to convert raw data numbers (DN) or engineering units (EU) from the telemetry from ATMS to calibrated radiances (antenna temperatures). The former (i.e. raw and minimally processed telemetry) are contained in the L0 data stream and forms the input to an L1a product generation element (PGE). The Level 1a products make up the input to the Level 1b PGE, while the output from the Level 1b process makes up the input to the Level 2 PGE, where the radiances are converted to geophysical parameters. This document describes calibration elements contained in the L1a and L1b processors. It does not describe geolocation, which is effected through an updated version of the EOS Toolkit. We emphasize that even though the L1b products make up the input to L2 processors, they are widely used by themselves, both in atmospheric research and in numerical weather prediction.

The algorithms described here are essentially the same as the Aqua AMSU ones and differ only minimally from those implemented by NOAA/JPSS, since the JPSS ATBD was derived from the NASA Aqua microwave ATBD. We note the following similarities and differences between the NASA terminology and NOAA terminology: L0 corresponds to RDR; L1b corresponds to SDR; L2 corresponds to EDR

The algorithms described in this document are very similar to those that have been developed by NOAA and NASA for the AMSU-A and -B instruments, which have flown since 1998 (NOAA) and 2002 (NASA), respectively. Details are based on the current Aqua AMSU-A/HSB

implementation. It is expected that this document will only be updated to reflect major revisions of the L1b code if there are changes in the theoretical basis or the formulation of the underlying algorithms. Since the basic functionalities and principles of operation of these instruments are quite similar, the differences between the respective algorithmic approaches are relatively minor. For example, while NOAA prefers to convert radiometer measurements to physical radiance units (mW/m^2-sr-cm^{-1}), the approach of NASA is to convert to brightness temperature units (K) instead, which is the most common practice in the microwave field. It is a simple matter to convert between the two.

It is the intention that this ATBD be readable as a standalone document, but *it is recommended that the reader reference related instrument and system description documents available from NGES, NGST, NOAA/JPSS and NASA*. In what follows there is a brief description of the instrument itself, in order to explain references to devices, procedures and tables used by the L1b algorithms. For a full understanding of the hardware and the measurement system, the reader should also refer to related CrIS and CrIMSS SDR/L1b and EDR/L2 ATBDs and similar documents, and the respective requirements documents and relevant hardware and software description documents. The present document reflects as-built performance characteristics to the extent they are known, and otherwise assumes full compliance of the hardware with the specifications.

This document describes the *functions* performed by the ground data system. However, it should be noted that nothing should be implied about the *architecture* or the *implementation* of the system. Thus, algorithms that may be described here as if they were to be executed in conjunction with each other could in fact be executed in isolation from each other. For example, data quality checking belonging to individual steps may be consolidated and executed before those step are reached in the actual processing system, in order to provide an efficient implementation. Also, in some instances there may be essential elements missing from the software implementation – those will be noted in the text and in a companion commentary.

Acknowledgments
Much of the illustrative material in this document has been provided by NGES.

1. Historical perspective

The Advanced Technology Microwave Sounder (ATMS), together with the Crosstrack Infrared Sounder (CrIS) — a high spectral resolution IR spectrometer — are designed to meet the measurement requirements set for the National Polar-orbiting Operational Environmental Satellite System (NPOESS), now succeeded by the Joint Polar Satellite System (JPSS), as well as satisfy the climate research needs of the National Aeronautics and Space Administration (NASA). The first version of this Crosstrack Infrared Microwave Sounding Suite (CrIMSS) was initially operated by NASA on the National Polar Partnership mission (NPP), previously called the NPOESS Preparatory Project, and later handed over to JPSS as an operational mission. NPP serves the two functions of providing risk reduction for JPSS and providing science data continuity between the NASA Terra and Aqua missions (the latter being the first mission to carry a high resolution sounding suite) on one hand and JPSS on the other. For that reason, the NPP mission has sometimes been called the "bridging mission". Additionally, while JPSS is primarily designed to support operational weather forecasting needs, NASA has a strong interest in research and climate applications, and an effort is under way to determine how JPSS can satisfy those needs as well. Thus, the third function of NPP is to serve as a testbed for transforming weather satellite data to climate research quality data.

The High Resolution Infrared Sounder (HIRS) and the Microwave Sounding Unit (MSU), together forming the TIROS Operational Vertical Sounder (TOVS) on the NOAA polar orbiting environmental satellite system (POES), have supported the National Weather Service (NWS) forecasting effort with global temperature and moisture soundings since the late 70's. In the course of the years HIRS has been periodically upgraded, and in 1998 a jump was made from MSU to the Advanced Microwave Sounding Unit (AMSU). The combined HIRS/AMSU system is called the Advanced TOVS (ATOVS) and has formed the backbone of the NOAA POES systems. It is expected to operate well into the NPP mission and possibly until the first JPSS mission proper (JPSS-1).

During the mid-1980's, while TOVS was still flying, it was determined that future numerical weather prediction (NWP) data needs would soon require satellite sounders with accuracies equivalent to radiosondes. An effort was launched by NASA to develop the technology and capability to achieve that. The result was the Atmospheric Infrared Sounder (AIRS), which, together with an AMSU microwave suite, was launched as part of the Aqua mission in 2002. AIRS was the first of a series of high spectral resolution IR sounders, and it has already demonstrated the utility of radiosonde quality satellite soundings – AIRS data is now being assimilated by a number of NWP centers and is having significant positive forecast impact. CrIS uses a different measurement approach (it is a Fourier transform spectrometer, while AIRS is a grating spectrometer), but it is the successor of AIRS and is expected to have comparable performance. Other instruments in the same class are being developed elsewhere.

During the mid-1990's, while AIRS was being built, an effort was made by NASA to transfer the AIRS technology to the Integrated Program Office (IPO), which was managing the NPOESS mission, with the goal of providing an AIRS follow-on for the NPOESS missions. Again, a technology development effort was launched – this time primarily focused on reducing the mass, size and power consumption of the microwave component of the sounding suite. The proposed

system – the Integrated Multispectral Atmospheric Sounder (IMAS) – was a single combined infrared and microwave instrument that was intended to fly as a demonstration on the NASA New Millennium Program's EO-3 mission. The effort was terminated in mid-1998 largely due to cost constraints, but many of the IMAS microwave specifications were later adopted for the ATMS instrument.

It was initially the intention to use the 118-GHz oxygen line for temperature sounding in the IMAS system, instead of the 50-60 GHz band used by AMSU. This would make it possible to shrink the aperture by a factor of more than 2 (and therefore also the overall mass and size) while maintaining spatial resolution and other performance measures. A field of view (FOV) of the same size as the IR sounder (i.e. 1.1°) was highly desired, and the IMAS/MW component was therefore designed to have that beam width for all sounding channels (i.e. in the 118-GHz band for temperature sounding and in the 183-GHz band for water vapor sounding). Later, it was realized that even the most transparent 118-GHz channels may not be able to penetrate to the surface under very humid and cloudy conditions (e.g., in the tropics), and the 50-GHz band was restored to provide backup capabilities for such situations. A compromise was made to use the same aperture size at 50 GHz as at 118 GHz, and a 2.5° beam width resulted. The IMAS team also determined that the microwave instrument should have the same spectral channels as AMSU for "science continuity" and that a few additional channels were desirable. Thus, two channels were added in the 183-GHz band, and one window channel was added in the 50-GHz band. In addition, the 150-GHz quasi-window channel used in AMSU-B was replaced with one at 166 GHz, which can be operated as part of an advanced-technology 183-GHz receiver (thus saving one receiver chain). This concept had been developed earlier by the AIRS team. Most of these specifications and characteristics are now part of the ATMS specifications, but the 118-GHz band was eliminated early in the program due to cost constraints, and 2.5° was changed to 2.2°.

The most significant advance under IMAS was the development of monolithic microwave integrated circuit (MMIC) technology at sounding frequencies (i.e. at 50, 118 and 183 GHz) – previously only available at considerably lower frequencies, which would allow for sensitive and compact receivers and spectrometers. Sample receivers were developed for the two lower bands, and low noise amplifiers (i.e. precursors to full receivers) were developed for the 183-GHz band, and compact solid-state filter banks were developed for the two lower bands. After the termination of IMAS these technology items were incorporated into an aircraft based microwave sounder, the High Altitude MMIC Sounding Radiometer (HAMSR), developed under the NASA Instrument Incubator Program. HAMSR may be viewed as an ATMS precursor and prototype in many respects (e.g., HAMSR uses a dual aperture, with two reflectors operating on a common axis, just as was later adopted for ATMS). HAMSR has been successfully operated on NASA high altitude aircraft since 2001. In summary, ATMS has heritage primarily from AMSU and from the IMAS design (and its HAMSR spin-off).

2. Instrument Description

In this section we give a brief description of the ATMS instrument, illustrated in Fig. 1. ATMS is
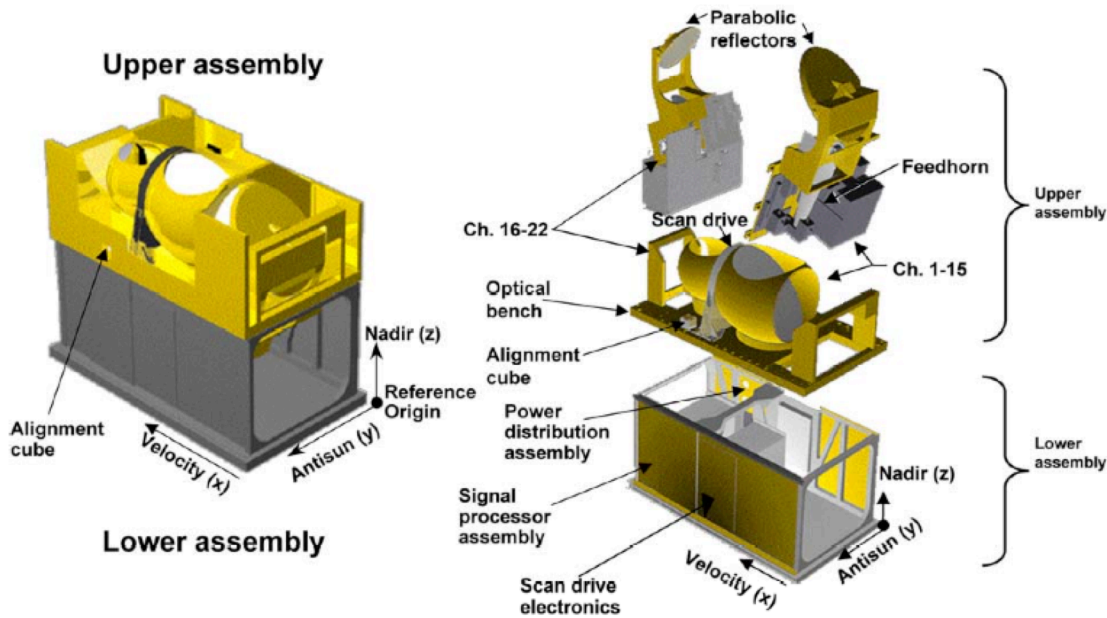

Figure 1: ATMS instrument layout

a 22-channel microwave sounder providing both temperature soundings – between the surface and the upper stratosphere (i.e. to about 1 mb, at an altitude of about 45 km) – and humidity soundings – between the surface and the upper troposphere (i.e. to about 200 mb, at an altitude of about 15 km). Like AMSU, it is a crosstrack scanner. There are two receiving antennas — one serving 15 channels below 60 GHz (with a beam width of 2.2° for all except the lowest two channels) and one serving 7 channels above 60 GHz (with a beam width of 1.1° for all except the lowest channel). The antennas consist of plane reflectors mounted on a scan axis at a 45° tilt angle, so that radiation is reflected from a direction perpendicular to the scan axis into a direction along the scan axis (i.e. a 90° reflection). With the scan axis oriented in the along-track direction, this results in a cross-track scan pattern. The reflected radiation is in each case focused by a stationary parabolic reflector onto a dichroic plate and from there either reflected to or passed through to a feedhorn. Each aperture/reflector therefore serves two frequency bands, for a total of four bands. Thus, radiation from a direction within the scan plane, which depends on the angle of rotation of the reflector, is reflected and focused onto the receiver apertures — conical feedhorns. This is illustrated schematically in Fig. 2.
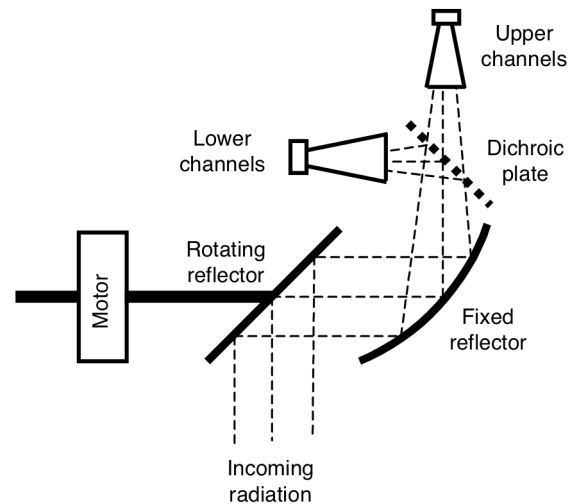
The design of the antenna system is such that a

Figure 2: ATMS antenna and RF feed subsystem (schematically): one of two

5

slightly diverging conical pencil "beam" is formed which has a half-power width (also called the 3-dB width) of either 1.1°, 2.2° or 5.2°, with a possible ±10% variation from channel to channel. Each beam is approximately Gaussian-shaped at the center and receives a significant portion of its energy outside the half-power cone. Approximately 95-97% of the energy is received within the so-called main beam, which is defined as 2.5 times the half-power beam width — i.e. the ATMS "main beam" is either 2.75°, 5.5° or 13° wide. Significant energy (i.e. up to 5%) is thus received from outside the main beam. Fig. 3 shows a typical antenna pattern. The pattern in the vicinity of the main beam is called the near sidelobes, while that further away is called the far sidelobes. The far sidelobes contribute significantly to the measurement errors.
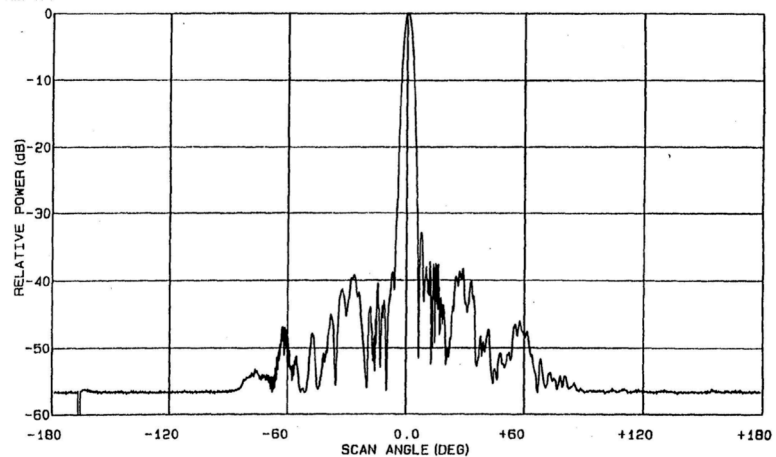
Figure 3: Typical microwave antenna pattern

The feedhorn is for some bands followed by a diplexer that splits the RF energy into two parallel signal paths that proceed to the respective receiver, which is in most cases a heterodyne system. There, each sub-band is down converted by a mixer, separated into channels with filters, and detected. Fig. 4 shows a block diagram of the ATMS system. In the following paragraphs we
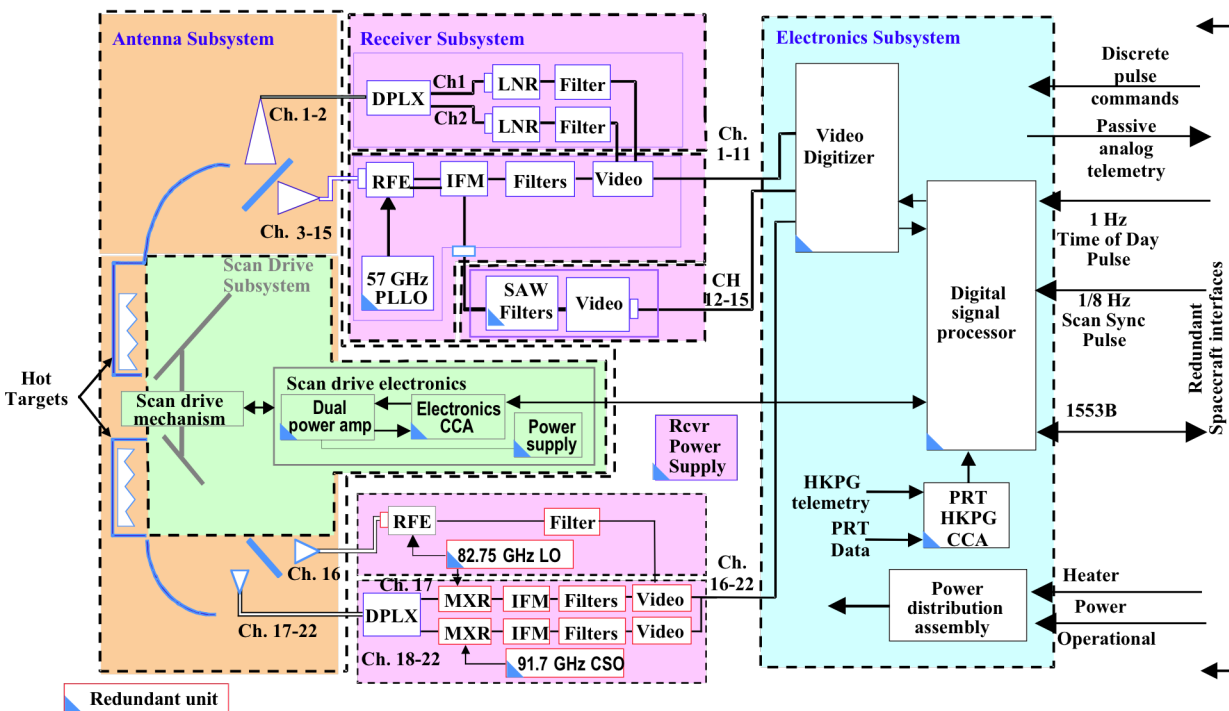

Figure 4. ATMS block diagram

will discuss the various signal paths that lead to the individual spectral channel outputs.

The larger of the two apertures is used for the 15 lowest-frequency channels and is some times referred to as the KAV-aperture, since it covers K-band (channel 1), Ka-band (channel 2) and V-band (channels 3-15). Here the dichroic plate, which reflects frequencies below a certain value and transmit those above, splits the RF energy into a low

Figure 5. Lowest-frequency receivers

frequency path (reflected) and a high frequency path (transmitted). The output of the low frequency feedhorn enters a diplexer, which in turn splits the now somewhat band limited RF energy into two parallel paths. Each is fed into an amplified receiver chain followed by a bandpass filter – one centered at 23.8 GHz (channel 1) and one centered at 31.4 GHz (channel 2). These are the only non-heterodyne receivers in the ATMS system. Fig. 5 illustrates this subsystem.
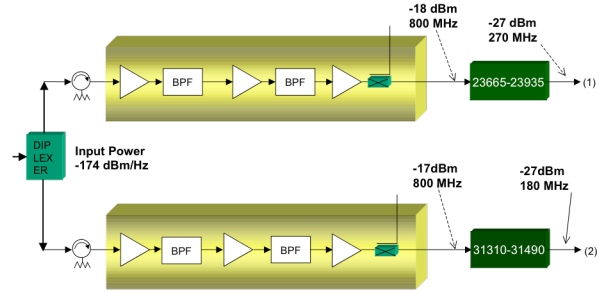
The output of the higher frequency feedhorn is fed into an amplified and bandpass filtered heterodyne receiver with two down-converter/mixer chains, both fed by a common local oscillator (LO) operating at 57.290344 GHz. (This is a highly stable and temperature controlled crystal referenced phase locked oscillator.) One path is low pass filtered, and the result is a single-sideband intermediate frequency (IF) band located at 1.6 – 7.1 GHz below the LO frequency. This band is in turn passed through a set of signal splitters/multiplexers and bandpass filters that select channels 3-9. The other path is bandpass filtered, and the result is a double-sideband IF band located 10 – 400 MHz away from the LO frequency. Two channels (10 and 11) are formed with conventional bandpass filters similar to those used for channels 3-9, while the rest (12-15) are formed with a standing acoustic wave (SAW) filter assembly. This is illustrated in Fig. 6. Note that the SAW assembly is implemented as a set of four pairs of filters, each positioned symmetrically with respect to an IF frequency of 322.2 MHz. The outputs of each filter pair are combined and amplified. Channels 12-15 are therefore in effect quadruple-sideband channels.
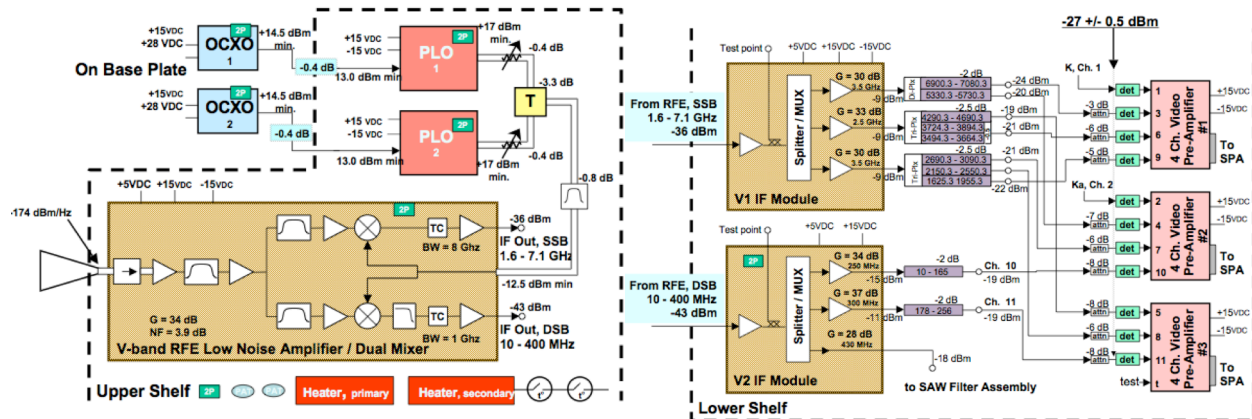

Figure 6. Channel 3-15 receiver subsystem

The smaller aperture is used for the 7 highest frequency channels and is some times referred to as the WG-aperture, since it covers W-band (channel 16) and G-band (channels 17-22). Here the lower frequency path (i.e. reflected from the dichroic plate) enters a single feedhorn and an amplified highpass filtered heterodyne receiver chain, where the mixer uses an LO operating at 82.75 GHz, producing a single upper sideband IF signal that is put through a 4450-6450 MHz bandpass filter for channel 16 (which results in a channel located at 87.2-89.2 GHz). The high frequency path (i.e. that transmitted through the dichroic plate) enters a smaller feedhorn followed by a diplexer that splits the signal into two paths. One path goes to a second harmonic mixer that uses the same LO as the channel 16 receiver. The resulting double sideband IF signal is put through a 350-1500 MHz bandpass filter for channel 17 (which is then located at 164-167 GHz with a gap at 165.15-165.85 GHz). The second path also goes to a second harmonic mixer, but it uses an LO operating at 91.655 GHz. The double sideband IF is passed through a set of filters that produce channels 18-22. (Those channels are therefore centered at 183.31 GHz $\pm$ Δf, where Δf is 7, 4.5, 3, 1.8 or 1 GHz, and the bandpass width varies from channel to channel.) This subsystem is illustrated in Fig. 7.
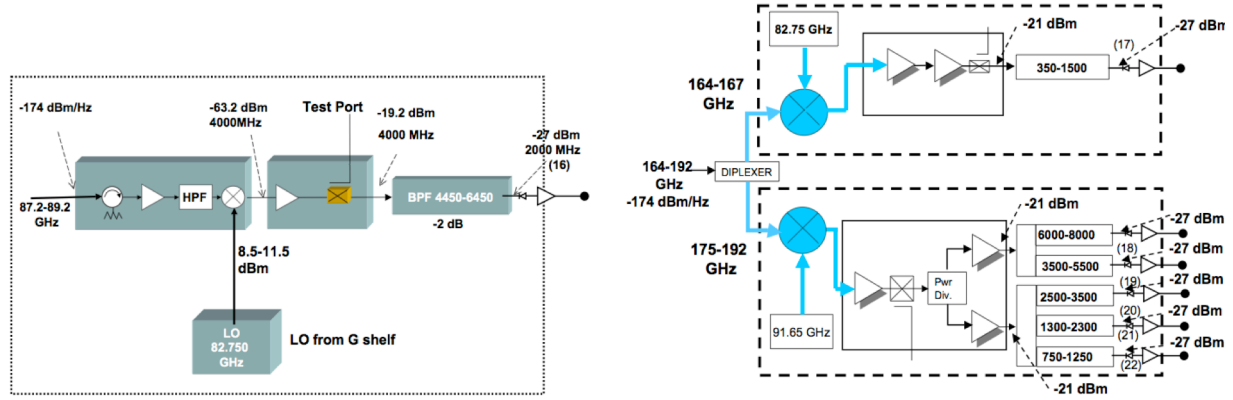
Figure 7. Channel 16 and 17-22 receiver subsystems

Table 1 summarizes the performance specifications of all 22 channels, including radiometric sensitivity – usually called noise equivalent temperature change and denoted as NEDT, which is listed in terms of specifications, measured performance on the ground and measured performance on-orbit. The table lists three frequency specifications: nominal center frequency, center frequency stability (i.e. the maximum deviation allowed from the nominal center frequency value), and specified and as-built bandwidth. All are given in MHz. The as-built bandwidth notation is "NxΔf", where N is the number of sub-bands used for a channel and Δf is the width of each sub-band. (E.g., 2x270 means this is a double-band channel, with each of the two bands being 270 MHz wide.)

Beamwidth and beam efficiency (computed from measured antenna patterns) are also listed. Finally, the polarization of each channel is listed. A single linear polarization is measured for each channel, and Table 1 lists the nominal polarization direction at the nadir scan position.

Ch	RF path			Center frequency [MHz]		Bandwidth [MHz]		NEDT [K]			Pol	Beamwidth [°]	Beam eff. [%]
	Ant	Feed	Rcvr	Value	Stab	Req	True	Req	T/V	Op'l		Req	
1	A	1	a	23800	<10	<270	1x270	0.5	0.2	0.2	V	5.2	99.6
2	A	1	b	31400	<10	<180	1x180	0.6	0.3	0.3	V	5.2	99.6
3	A	2	c	50300	<10	<180	1x180	0.7	0.4	0.3	H	2.2	99.4
4	A	2	c	51760	< 5	<400	1x400	0.5	0.3	0.3	H	2.2	99.5
5	A	2	c	52800	< 5	<400	2x170	0.5	0.3	0.3	H	2.2	99.5
6	A	2	c	53596±115	< 5	170	1x170	0.5	0.3	0.3	H	2.2	99.4
7	A	2	c	54400	< 5	400	1x400	0.5	0.3	0.3	H	2.2	99.5
8	A	2	c	54940	<10	400	1x400	0.5	0.3	0.3	H	2.2	99.5
9	A	2	c	55500	<10	330	1x330	0.5	0.3	0.3	H	2.2	99.5
10	A	2	d_1	57290.344 [f_0]	<0.5	330	2x155	0.75	0.4	0.4	H	2.2	99.5
11	A	2	d_1	f_0±217	<0.5	78	2x 78	1.0	0.5	0.5	H	2.2	99.5
12	A	2	d_2	f_0±322.2±48	<1.2	36	4x 36	1.0	0.6	0.5	H	2.2	99.5
13	A	2	d_2	f_0±322.±22	<1.6	16	4x 16	1.5	0.8	0.8	H	2.2	99.5
14	A	2	d_2	f_0±322.±10	<0.5	8	4x 8	2.2	1.2	1.1	H	2.2	99.5
15	A	2	d_2	f_0±322.±4.5	<0.5	3	4x 3	3.6	1.8	1.8	H	2.2	99.5
16	B	3	e	88200	<200	2000	1x2000	0.3	0.3	0.3	V	2.2	97.7
17	B	4	f	165500	<200	3000	2x1150	0.6	0.4	0.4	H	1.1	97.8
18	B	4	g	183310±7000	<30	2000	2x2000	0.8	0.3	0.4	H	1.1	97.8
19	B	4	g	183310±4500	<30	2000	2x2000	0.8	0.4	0.4	H	1.1	97.9
20	B	4	g	183310±3000	<30	1000	2x1000	0.8	0.5	0.5	H	1.1	98.5
21	B	4	g	183310±1800	<30	1000	2x1000	0.8	0.5	0.5	H	1.1	98.5
22	B	4	g	183310±1000	<30	500	2x 500	0.9	0.7	0.7	H	1.1	98.5

Because of the rotating main reflector, the detected polarization vector rotates as the scan reflector rotates. (This can be understood by envisoning the detected polarization vector, which is fixed relative to the feedhorn, being projected onto the ground below – by simple geometric imaging.) The direction indicated in Table 1 as "V" corresponds to a direction that lies in the scan plane, while "H" is the direction that is perpendicular to the scan plane – i.e. in the horizontal plane. (At nadir these two polarizations are degenerate, i.e. observed emissions would be identical for an isotropic surface.) As the scanner rotates the beam away from nadir, the detected "V" polarization also rotates out of the scan plane while the detected "H" polarization rotates out of the perpendicular plane and thus also out of the horizontal plane. The angle of rotation away from the respective planes equals the scan angle relative to nadir. This is illustrated schematically in Figure 8, which shows the projection of the various polarization vectors in the plane perpendicular to the ray path (i.e. the plane that contains the electromagnetic field vectors). This plane coincides with the horizontal plane for the nadir scan position but rotates as the scan position rotates. In addition, as explained above, the "H" and "V" polarization vectors rotate within this plane. When surface emissivity and similar quantities are computed, it is important to correctly transform between the observed "H" and "V" vectors and the local true H and V vectors as computed from models.

The antenna reflectors rotate continuously counter-clockwise relative to the
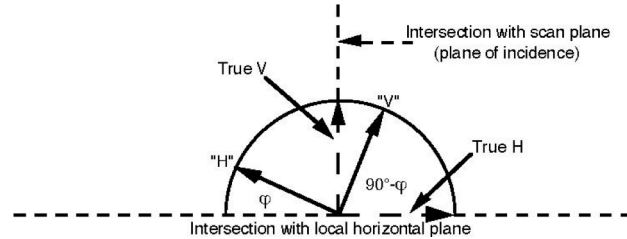
Figure 8. Polarization vectors, in the transverse plane

spacecraft direction of motion (i.e. the spin vector points in the negative x-direction while the spacecraft moves along the positive x-direction), completing three revolutions in 8 seconds. The scan mechanism is synchronized to the spacecraft clock with a "sync" pulse every 8 seconds (i.e. for every third revolution). Each scan cycle is divided into three segments. In the first segment the earth is viewed at 96 different angles, symmetric around the nadir

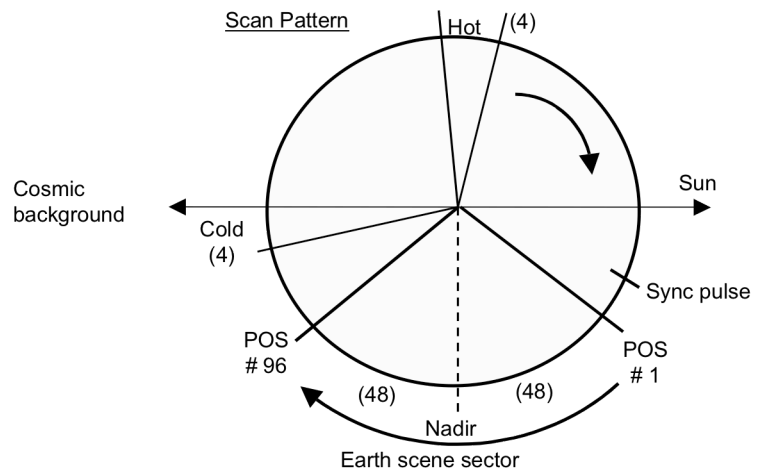**Figure 9.** Scan sequence (flight direction is toward the reader)

direction. The antenna is in continuous motion, and the 96 samples are taken "on the fly", with each sample representing the mid-point of a brief sampling interval of about 18 ms. The scan speed is such that the corresponding angular sampling interval is 1.11° (i.e. the scan speed is about 61.6°/second). The angular range between the first and last sample centroids is therefore 105.45° (i.e. ±52.725° relative to nadir). The antenna then accelerates and moves to a position that points it toward an unobstructed view of space (i.e. between the earth's limb and the spacecraft horizon). There it resumes the same slow scan speed as maintained across the Earth scenes while four consecutive cold calibration measurements are taken. Next, the antenna is again accelerated to the zenith direction, which points it toward an internal calibration target that is at the relatively high ambient instrument temperature, and is again slowed down to normal scan speed while four consecutive warm calibration measurements are taken. Finally, it is accelerated to the starting Earth scene position, where it is slowed down to normal scan speed to begin another scan cycle. Every third cycle the synchronization signal arrives just before the start position is reached and is used to maintain this pattern through a phase locked loop. Fig. 9 illustrates this — the normal operational scan mode. (There is also a stare mode, where the antenna can be pointed to the nadir direction or either of the calibration directions for an extended period of time, but that is only used for special purposes.) Each of the 96 earth samples takes about 18 milliseconds, for a total of approximately 1.73 seconds. The "duty cycle" of ATMS is therefore about 65%, i.e. about 65% of the scan cycle period is dedicated to Earth observations.

As of this writing, a major change in the scan profile was under consideration by JPSS, which now has operational responsibility. The purpose is to attempt to extend the expected life time of ATMS by reducing stresses on the scan system caused by the large accelerations and decelerations of the current scan profile. If this is implemented, this section of the ATBD will be updated to reflect the changes.

Instrument Interoperability Issues

As described earlier, the CrIS/ATMS instrument suite forms a single sounding system, CrIMSS, even though it consists of two independent instrument modules, and the retrieval approach is based on the assumption that the two instruments are viewing the same air mass and surface "footprint" at the same time. This requires both alignment and synchronization. The details are beyond the scope of this document, and here we will simply point out that there are differences between the operational aspects of CrIS and ATMS that present challenges to achieving this goal. For example, CrIS completes a single scan cycle in 8 seconds, with 30 samples of a 3x3 cluster of individual FOVs and each cluster separated by 3.33°. While the resulting spatial sampling density is nearly identical to that of ATMS, their scan speeds differ markedly (i.e. three vs. one scan cycle every 8 seconds), which causes significant alongtrack misalignment at the scan swath edges. Alignment could have been optimized (but not made perfect, due to the fact that the CrIS 3x3 sample cluster rotates with scan angle in a manner similar to that of the ATMS polarization vectors) by mounting CrIS with a slight (less than 1°) positive yaw angle relative to ATMS (or mount ATMS with a negative yaw relative to CrIS), but that has not been done. Synchronization is more easily achieved, by introducing a time offset between the occurrence of the 8-second sync pulse and the start of a new scan cycle (which is defined as the start of the first Earth sample interval). ATMS has been designed to allow for such a delay, with a value that can be commanded from the ground, but this is also not done. The objective of co-alignment and synchronization is usually to achieve close spatial coincidence between the respective "footprint" patterns projected on the ground. The AIRS-AMSU system incorporates both a yaw correction and synchronization, but the HIRS-AMSU system does not, nor does CrIS-ATMS. Instead, "co-alignment" must be done as part of ground processing, through interpolation or other resampling. NOAA/JPSS has implemented a Backus-Gilbert resampling scheme as part of the TDR-to-SDR step, but NASA will defer that to be incorporated into L2 processing or possibly a pre-L2 step. (Similarly, NOAA/JPSS imlements scan bias correction in the SDR step, while NASA will defer that as well to L2 or pre-L2.)

3. In-flight Calibration System

As described in Section 2 (Instrument description), and illustrated in Fig. 9 (scan sequence), each of the two ATMS antenna/receiver systems measures the radiation from two calibration sources during every scan cycle. The first source is the cosmic background radiation emanating from space. This source is viewed immediately after the earth has been scanned. The antenna is quickly moved to point in a direction between the earth's limb and the spacecraft's horizon. There it drifts slowly while 4 measurements are taken. The second source is an internal blackbody calibration target (often called a "warm load"), which is at the ambient internal instrument temperature (typically, 0-15° C). This source is viewed immediately after the space calibration view; the antenna is again quickly moved, to point in the zenith direction, where the blackbody target is located. Again, the antenna drifts slowly while 4 measurements are taken. Thus, two sets of calibration measurements that bracket the earth scene radiances are obtained for every scan cycle. A full discussion of calibration issues can be found in a document produced by NGES[1].

Such a through-the-antenna calibration system allows most system losses and instrument defects to be calibrated out, since the calibration measurements involve the same optical and electrical signal paths as earth scene measurements. (The only exception is that the internal calibration target appears in the antenna near field and can reflect leakage emission from the antenna itself. That effect is taken into account with bias corrections in the calibration processing, however.) This approach has an advantage over calibration systems using switched internal noise sources injected into the signal path behind the antenna, at the cost of some weight gain since the internal calibration target is fairly massive.

The purpose of the calibration measurements is to accurately determine the so-called radiometer transfer function, which relates the measured digitized output (i.e. counts, C) to the associated radiometric "brightness" temperature:

$$\mathcal{T}' = \mathcal{F}(C) \qquad\qquad\qquad (3\text{-}1)$$

This function, which is illustrated schematically in Fig. 10 (and where the subscripts c and w refer to the cold and warm calibration points, respectively, and s refers to an Earth scene) depends primarily on channel frequency and instrument temperature, but it could also undergo short term and long term changes due to gain fluctuations and drift due to aging and other effects. Note that others, notably NOAA, use the physical quantity called radiance, which has units of mW/m^2-sr-cm^{-1}, instead of the quantity called brightness temperature that we will use here, which has units of K. It is a
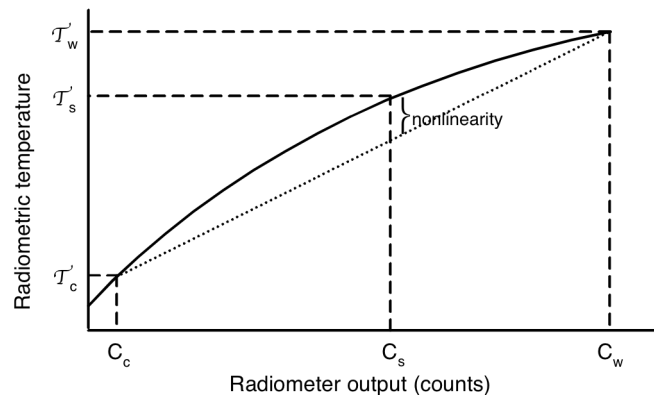

Figure 10. Transfer function schematically

---

[1] "ATMS Radiometric Math Model", NGES Report 12110 (2004)

simple matter to convert between the two, however.

If the transfer function were perfectly linear, then two calibration points would uniquely determine its form at the time of the calibration measurements, since two coefficients could then be computed:

$$\mathcal{F}_{lin}(C) = a_0 + a_1 C \tag{3-2}$$

While it has been a design goal (and a requirement) to make the transfer function as linear as possible, in reality it is slightly nonlinear. To account for the slight nonlinearities we allow for a quadratic term:

$$\mathcal{F}_{nonlin}(C) = a_0 + a_1 C + a_2 C^2 \tag{3-3}$$

The magnitude of the quadratic nonlinearity is of course zero at the two calibration points and its functional form can therefore be uniquely expressed as

$$\mathcal{T}'_{NL} = 4x(1-x)\, T_{NL} \tag{3-4}$$

where x is a measure of the relative distance of an Earth scene point from the two calibration points,

$$x = (\mathcal{T}'_s - \mathcal{T}'_c)/(\mathcal{T}'_w - \mathcal{T}'_c) \tag{3-5}$$

and T_{NL} is the peak nonlinearity, occurring at the midway point, i.e. at $x = 0.5$.

We emphasize that these expressions pertain to a quadratic nonlinearity model – which is thought to be a good approximation, since the nonlinearities are generally quite small. We also note that determining T_{NL} from ground measurements is not straightforward, and detecting changes in its value after launch (a distinct possibility) is even more difficult. In principle, this parameter may be a function of instrument temperature and may have other dependencies as well. The current algorithm allows the choice of using a fixed set of nonlinearity terms or determining those terms as a function of the instrument temperature and the PLLO redundancy configuration. The receiver shelf temperature (KKA Shelf, V Shelf, W Shelf, and G Shelf) is used to interpolate between table pairs determined from pre-launch test data. Each table pair consists of a receiver temperature and a nonlinearity term.

For AMSU, the form given in Eq. 3-3 was used, both by NOAA and by NASA, and the calibration algorithms specified how the coefficients a_0-a_2 were to be computed. The approach used by JPSS for ATMS is to first use the linear approximation (equivalent to Eq. 3-2) and then make a quadratic correction per Eq. 3-4. The linear approximation is simply a representation of a straight line through the two calibration points (the dotted line in Fig. 10):

$$\mathcal{T}'_{lin} = \mathcal{T}'_c + [(\mathcal{T}'_w - \mathcal{T}'_c)/(C_w - C_c)]\,(C - C_c) \tag{3-6}$$

i.e. the linear coefficients are

$$a_1 = (\mathcal{T}'_w - \mathcal{T}'_c)/(C_w - C_c) \qquad (3\text{-}7)$$

$$a_0 = \mathcal{T}'_c - a_1 C_c \qquad (3\text{-}8)$$

The inverse of a_1 is often called the "gain", an important measure of radiometer output for a given scene temperature:

$$g = 1/a_1 = (C_w - C_c)/(\mathcal{T}'_w - \mathcal{T}'_c) \qquad (3\text{-}9)$$

In the following paragraphs we first discuss how the calibration points are obtained. Subsequent sections discuss how the Earth scene brightness temperatures are determined.

3.1 Blackbody view

The internal calibration targets are approximately cylindrical in outline and are made up of pyramid shaped metal structures coated with an absorbing material. Figure 11 shows an AMSU calibration target (the ATMS targets are quite similar). For the larger aperture, the pyramids are about 1 cm across and about 4 cm high. The metal base and core ensures that temperature gradients across the targets are minimal, while the pyramid structure and the absorbing coating ensure that the emissivity is close to 1. The target is surrounded by a metal shroud, which mates very closely with a matching shroud surrounding the rotating reflector antenna, to prevent stray radiation from external sources from affecting the warm calibration measurements. For ATMS, where the antenna moves during calibration measurements, the calibration target is slightly larger than the antenna shroud aperture, so that the antenna has a full view of the target during the entire calibration period.
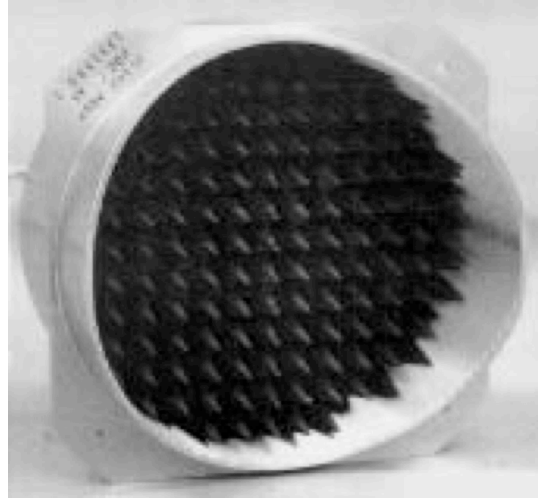

Figure 11. Typical warm load

In order to reduce the effect of random noise, the calibration target is viewed four times consecutively. (Consecutive samplings are used in lieu of a single sampling of longer duration in order to keep the data collection control system simple.) The effective calibration measurement noise, after averaging, is then reduced by a factor of 2 below the NEDT values listed in Table 1. These values can be reduced even further by averaging over several calibration cycles, as we will describe in Section 5. The four consecutive measurements are assumed to be entirely equivalent, but that assumption remains to be tested, both on the ground and on-orbit. (The calibration algorithms may have to be modified if this assumption turns out to be faulty.)

The emissivity of the calibration targets is required to be at least 0.9999. This is necessary in order to keep radiation that is unavoidably emitted from the radiometer's local oscillators through the antenna and reflected back from the calibration target to a minimum. (Such radiation could masquerade as a radiated brightness temperature of as much as 100 K. An emissivity of 0.9999, and thus a reflectivity of 0.0001, would then yield a reflected contribution of 0.01 K – a negligible amount.) Measured ATMS target emissivities exceed 0.9999, and maximum emission from the antenna has been measured to be less than 100 K (using a "tunable short test").

The targets are not thermally controlled, but since they are somewhat insulated from external thermal swings (and the entire instrument is thermally insulated from the platform), it is expected that the target temperatures will not change rapidly (less than 0.001 °C/sec) and that temperature gradients across the targets will be minor (less than ±0.05 °C). To ensure good knowledge of the target temperatures, there are 7-8 temperature sensors (Platinum Resistance Thermometers — PRT's) embedded throughout each of the two targets. Measurement accuracy is better than 0.1 °C. The PRT's are embedded in the metal structure from the back, close to the coated front surface.

One potential problem is that any vertical temperature gradient in the pyramid structure will not be measured and is also difficult to model and predict. There are indications from previous studies that such gradients can have a major effect on calibration accuracy, particularly because they are thought to be frequency dependent (i.e. radiation at the shorter wavelengths may originate from a particular part of the pyramids while longer wavelengths may originate from a different area – e.g., tips vs. troughs). Temperature gradients in a periodic structure as in the ATMS targets can also cause resonant effects such as grating "sidelobes". The performance on-orbit may therefore be somewhat poorer than as measured on the ground (where benign and controlled conditions are usually maintained). Bias corrections determined from thermal-vacuum tests on the ground may compensate for some of these effects, however.

In general, there will be a small difference between the brightness temperature computed from the physical temperature of the target and its estimated emissivity on one hand and the brightness temperature inferred from the radiometer output on the other. This is caused by effects such as discussed above. One of the objectives of the ground based thermal-vacuum measurements, where operational conditions are simulated as closely as possible, is to determine the magnitude and dependencies of such biases. This is accomplished by observing a NIST-traceable reference target in lieu of an Earth "scene". Since the brightness temperature of such a target is known with better accuracy than that of the ATMS internal warm loads, it is possible to use it to infer the warm load biases discussed here. Such biases are typically quite small but may be of the same magnitude as the target calibration accuracy and must therefore be accounted for in the calibration processing. The biases, i.e. observed differences between inferred ATMS warm load brightness temperatures and known simulated scene brightness temperatures, may depend on the physical temperature of the receiver system.

3.2 Cold space view

For the other calibration data point the cosmic background radiation is also sampled four times consecutively. Here, however, the radiative environment is much more complex than for the warm calibration target view. Although the cosmic radiometric temperature is well known (2.726 ± 0.004 K), significant radiation from the earth as well as earth radiation reflected from spacecraft structures can enter the antenna sidelobes. This is illustrated conceptually in Figure 12, where we have superimposed a polar plot of a typical antenna pattern over a schematic picture of the viewing geometry. (The example is from AMSU, which has a broader beam

Figure 12. Space view geometry
(flight direction is toward the reader, out of the page)

than most ATMS channels, but this is for illustrative purposes.) As a general rule, we can estimate that on the order of .1-.2 % will be received from the 125° sector that "sees" Earth from an 825-km orbit altitude. This contribution is then on the order of 1/4-1/2 K, i.e. about 1/10th-1/5th of the cosmic radiation. This is not insignificant, but the effect on calibration accuracy is relatively small, as discussed in the next section. Contributions due to reflections from the structures and surfaces on the spacecraft are probably minor. (Radiation emitted from the spacecraft is expected to be negligible, since most surfaces will be covered with MLI blanket – a metallized Mylar material that is highly reflective at microwave frequencies.)
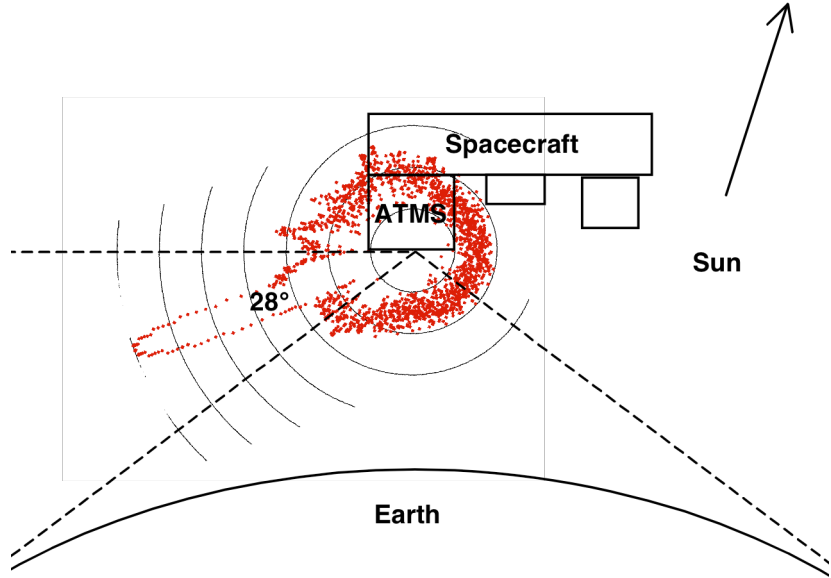
Figure 12 also suggests that the Earth sidelobe radiation probably depends on the exact pointing direction and is likely to be greatest when the antenna boresight is closest to Earth. This means that, for a given nominal space calibration position, the sidelobe contribution may vary between the four consecutive samples – which cover an angular range in excess of 4°. The baseline algorithm averages these together to reduce the effective noise, but analysis must be undertaken after launch to determine if that is appropriate (just as a similar analysis is required for the warm calibration measurements).

It is common practice to use the Rayleigh-Jeans approximation for brightness temperature, which is essentially that (ignoring the emissivity) the brightness temperature equals the physical temperature,

$$\mathcal{T}' \approx T \tag{3-10}$$

This is a low-frequency high-temperature approximation that breaks down for combinations of high frequency and low temperature, which is the case for ATMS in the context of the low brightness temperatures normally encountered during cold calibration. To correct for the resulting error, it is common practice in the microwave community to use the so-called thermodynamic definition of brightness temperature,

$$\mathcal{T}' = (hf/k)\{0.5 + [\exp(hf/kT) - 1]^{-1}\} \tag{3-11}$$

At the low-frequency high-temperature limit, this expands as one would expect to

$$\mathcal{T}' = T + 0.5 \, hf/k + \text{higher order terms} \tag{3-12}$$

At cold-space temperatures there is therefore a small correction term, hf/2k, but at normal scene temperatures the 'higher order terms' will cancel it out. The correction term is usually only applied to the space view. At higher but sub-normal scene temperatures, such as the 80 K that can be encountered in reality, Eq. (3-12) should also properly be applied, but that is rarely done.

Finally, we should note that the cold space view can also be contaminated by the Moon. From time to time (i.e. on a quarterly cycle) the Moon, which is near half-full when seen from the spacecraft, may approach the field of view of one of the space view positions. The worst-case effect, i.e. with the Moon exactly in the boresight direction, is to elevate the space view brightness temperature by up to 20 K for the channels with a 1.1° FOV, up to 5 K for the channels with a 2.2° FOV and 1 K for the channels with a 5.2° FOV. Also in the worst case, the effect may be detectable for a period up to 10 minutes. When this happens, it is necessary to either account for the increase in space view brightness temperature (i.e. model it) or reject the observation from calibration processing based on prediction or detection.

3.3 Sources of errors and uncertainties

In this section we summarize the sources of errors and uncertainties in the calibration process. A detailed analysis can be found in the NGES "Radiometric Math Model" report referenced earlier.

Errors can be classified as systematic (bias) errors, which are uncertainties in the bias corrections applied, and random errors, which are uncertainties due to random fluctuations of the instrument characteristics. We will in general correct for all known biases, so that only their uncertainties remain. We assume that all uncertainties are independent and random and add up in a root-sum-squared (rss) sense. (This is not strictly correct, but the resulting errors in the uncertainty estimates are judged to be relatively small.)

As was explained in the introductory part of this section, the in-flight calibration procedure consists of determining the transfer function at two points — the cold space calibration view and the internal blackbody calibration view — and fixing a quadratic function between these two anchor points, where the amplitude of the quadratic deviation from linearity (denoted by T_{NL} in

Eq. 3-4) is assumed to be fixed for each channel and possibly a function of instrument temperature. The transfer function thus determined is then used to convert earth scene radiometer measurements to a corresponding brightness temperature. The absolute accuracy of this scene brightness temperature is termed the calibration accuracy. (*Calibration accuracy* is strictly defined as the difference between the means of the inferred and the actual brightness temperature when a blackbody calibration target is placed directly in front of the antenna for an extended period of time.) It can be expressed as

$$\Delta T'_b = \text{RSS}\{x\Delta T'_w \; ; \; (1-x)\Delta T'_c \; ; \; 4x(1-x)\Delta T_{NL} \; ; \; \Delta T'_{sys}\} \tag{3-13}$$

where "RSS" means that the result is the square root of the sum of the squares of the terms. The factor x is the relative scene temperature defined in Eq. 3-5, and $\Delta T'_w$, $\Delta T'_c$, and ΔT_{NL} are the respective uncertainties in the calibration radiometric temperatures and the nonlinearity amplitude. $\Delta T'_{sys}$ is an uncertainty due to random instrument fluctuations (e.g., gain fluctuations). Note that no biases are included in Eq. (3-13); it expresses the uncertainty only.

Although scene temperatures may go as low as 80-90 K at the higher frequencies, the meaningful operational dynamic range is 200-300 K for sounding channels and about 140-300 K for window channels. Substantially lower sounding temperatures are caused by scattering from raindrops or ice above precipitating cells – conditions that currently cause the retrieval process to fail. (It is possible that scattering may be included in the retrieval algorithms in the future, however.) Very transparent window channels, where a low ocean emissivity makes ocean scenes appear radiometrically very cold, are also not crucial to the retrieval processing. Thus, the effective meaningful dynamic range is 200-300 K. With a T'_w on the order of 300 K and T'_c close to zero, the meaningful dynamic range for x is 2/3–1. In the worst case (x~2/3) the relative weights of the first two terms in Eq. 3-13 are then 4/9 and 1/9, respectively. This means that errors in T'_c contribute 4 times less to the overall calibration accuracy than errors in T'_w, and for most scenes considerably less than that. It is useful to keep this perspective in mind when the error sources are discussed.

In the following we will briefly discuss the factors contributing to the uncertainties. The interested reader is referred to the Radiometric Math Model document for a thorough and detailed discussion.

Blackbody error sources
These errors stem from *uncertainty* in the knowledge of four factors:
 a) blackbody emissivity
 b) blackbody physical temperature
 c) reflector/shroud coupling losses
 d) reflected local-oscillator leakage
Of these, the second term is expected to dominate.

The *emissivity* is generally known to lie in a range, [ε_{min}, 1.0], due to limited measurement accuracy. (A typical value for ε_{min} is 0.99993.) This should be interpreted as

$$\varepsilon = 1.0 - (1.0 - \varepsilon_{min})/2 \pm \Delta\varepsilon \qquad (3\text{-}14)$$

where $\Delta\varepsilon$ is the estimated uncertainty. It is bounded by $(1.0 - \varepsilon_{min})/2$. (For the example quoted, where ε_{min} is estimated to be 0.99993, the uncertainty would be estimated at < 0.000035.) An alternative estimate could be based on an analysis of the method used to determine the emissivity (typically by measuring the reflectivity).

The *blackbody physical temperature* is uncertain due to
   a) surface temperature drifts between the time of temperature measurement and the time of radiometer measurement (ΔT_{drift})
   b) temperature gradients in the blackbody (ΔT_{grad})
   c) temperature measurement uncertainties (ΔT_{meas})
   d) vertical gradients and uncertain origin of the radiation (ΔT_{vert})
The last factor is currently unknown, but it is possible it may dominate this term.

The *reflector/shroud coupling losses* occur because the antenna and blackbody shrouds do not mate perfectly, and external radiation (from the interior of the instrument) will enter the antenna through the gap between the shrouds. This effect is uncertain because of uncertainties in measuring and modeling the coupling losses as well as uncertainties in the knowledge of the external radiation. The magnitude of this is expected to be very small and can be ignored.

Finally, the *leakage* signal originating from the local oscillators and emitted by the antenna may be reflected back to the antenna by the blackbody, if its emissivity is not unity (i.e. if its reflectivity is not zero). This is uncertain because the leakage signal is not known precisely and the target reflectivity (or emissivity) is not known precisely. The latter is expected to dominate, and the former can be ignored. (The reflected LO signal may also interfere with itself by changing the operating point of the detector system, which then impacts the intrinsic noise level of the amplifier. Thus, although the LO interference may be well outside the IF passband and therefore not directly measurable, it can still significantly impact the apparent output noise of the system.)

The resulting uncertainty is

$$\Delta\mathcal{T}'_w = \text{RSS}\{\Delta\varepsilon\,\mathcal{T}'_w;\ \Delta T_{drift};\ \Delta T_{grad};\ \Delta T_{meas};\ \Delta T_{vert};\ \Delta\varepsilon\,\mathcal{T}'_{LO}\} \qquad (3\text{-}15)$$

where $\mathcal{T}'_{LO}$ is the leakage radiance, expressed as a brightness temperature.

Only the first term is expected to change in orbit, so this can be contracted to

$$\Delta\mathcal{T}'_w = \{[\Delta\varepsilon\,\mathcal{T}'_w]^2 + [\Delta T_{w,fixed}]^2\}^{1/2} \qquad (3\text{-}16)$$

where $\Delta T_{w,fixed}$ represents the unchanging terms compiled from ground measurements.

Cold calibration (space view) error sources

This error stems from uncertain knowledge of three factors:
   a) Earth contamination through the antenna sidelobes
   b) spacecraft contamination through the antenna sidelobes
   c) the cosmic background temperature

The *sidelobe contamination* is uncertain due to uncertain knowledge of the antenna pattern (i.e. sidelobes) as well as uncertain knowledge of the radiation from Earth and from the spacecraft. (The latter consists mostly of reflected Earth radiation, since most visible surfaces will be covered by reflective materials, as discussed above.) Both effects may be modeled and pre-computed, but the associated uncertainties are expected to be substantial. This is the largest contribution to this term.

We may express the sidelobe radiation as the product of an effective antenna efficiency, a_{eff}, (over the sector that receives this radiation) and an effective scene temperature for that sector, T'_{eff}:

$$T'_{SL} = a_{eff} T'_{eff} \qquad (3\text{-}17)$$

The uncertainty is then the sum of two terms,

$$\Delta T'_{SL} = RSS\{\Delta a_{eff} T'_{eff} \; ; \; a_{eff\Delta} \Delta T'_{eff}\} \qquad (3\text{-}18)$$

The uncertainty in a_{eff} is primarily due to uncertain antenna patterns (from which it is usually computed), and the uncertainty in T_{eff} is primarily due to an uncertain or variable mean brightness temperature of the visible Earth disc. There is also an error component caused by representing the sidelobe radiation as the simple product shown in Eq. 3-17 – in reality this is a double integral, i.e. a convolution between the two. It may be noted that the effective scene temperature varies along the orbit – there are both latitudinal (i.e. intra-orbital), longitudinal (i.e. inter-orbital) and temporal (e.g., inter-seasonal) variations in the effective brightness temperature of the visible portion of the Earth. This may be modeled or estimated in other ways, or it may be ignored and instead carried as an additional uncertainty.

Finally, although the *cosmic background temperature* is well known, there is an uncertainty associated with it. However, it can be ignored here, since the uncertainty of the sidelobe radiation is expected to dominate the cold calibration uncertainty. The result is

$$\Delta T'_c \approx \Delta T'_{SL} = RSS\{\Delta a_{eff} T'_{eff} \; ; \; a_{eff\Delta} \Delta T'_{eff}\} \qquad (3\text{-}19)$$

Instrument (transfer function) error sources
This error stems from uncertainty in the knowledge of four factors:
   a) nonlinearities
   b) system noise
   c) system gain drift
   d) bandpass shape changes

The *nonlinearities* can be modeled as a quadratic term that may be a function of a characteristic instrument temperature, as discussed above. This is only an approximation and is therefore uncertain. In addition, as for the blackbody, the instrument temperature is not known precisely. We will, however, ignore the latter effect. The former is expressed in terms of the uncertainty of the peak nonlinearity, ΔT_{NL} in Eq. (3-13).

The system terms are due to random fluctuations and are characterized in terms of standard deviations. These are channel dependent, as are most of the effects discussed above. The combined effect is expressed as $\Delta Tsys$ in Eq. (3-13).

4. Processing parameters and tables

The manufacturer of the instrument (NGES) was required to carry out an extensive suite of tests, to demonstrate compliance with performance requirements as well as to characterize the as-built performance. All test results and associated data which may be relevant to postlaunch calibration and data processing are organized in a calibration log book, which contains information on the following aspects, among others:

- PRT calibration coefficients (to convert A/D counts to temperature)
- Antenna pointing data (resolver count vs. intended and actual position)
- Antenna patterns (360° scans in 4 cuts, selected positions, co- & cross-pol.)
- Bandpass filter data
- Thermal-vacuum tests (radiometric performance vs. instrument temperature)

From the data supplied in the calibration log book and other sources various parameters and tables have been generated to be used for routine data processing. They may be updated from time to time. Table 2 contains a list of such parameters.

Table 2. Processing paramters

Symbol	Function	No. of items	Section
Calibration parameters			
R_0, α, β, δ	Callendar-Van Dusen PRT coefficients	4 per PRT	L1a
$c_0 - c_3$	Alternative PRT coeff's	4 per PRT	L1a
a, b, c	BB temp. bias correction	3 per channel (22) per PLLO (2)	5.1.1.i
$\Delta\mathcal{T}'_w$	Alternative BB temp. bias correction	1 per band (5)	
b_0, b_1	BB radiometric temperature correction	2 per channel	5.1.2.a
ε	BB emissivity	1 per channel	5.1.2.b
ΔTb_{SL}	SV sidelobe contamination	1 per SV position (4), per channel and per location/time (var)	5.2.4
W	Cal-count smoothing function	N per channel	5.4.2-3
u	Nonlinearity coefficient	1 per channel and per instrument temp	5.5.2
Quality check parameters			
T_{min}, T_{max}	BB PRT limits	1 pair per PRT	5.1.1.b
ΔT_{max1}	Max. BB PRT difference in a cal. cycle	1 per BB (2)	5.1.1.c
ΔT_{max2}	Max. BB PRT difference between cal. cycles	1 per BB	5.1.1.e
N_{min}	Min. number of good PRT readings in a cal. cycle	1 per BB	5.1.1.d
T_{low}, T_{upp}	RF shelf PRT limits	1 pair per rcvr (5)	5.1.1.i
ΔT_{rmax}	Max. RF shelf difference between cal. cycles	1 per rcvr	5.1.1.i
α_{max}	Lunar contamination half-cone angle limit	1 per SV (4x4) and per apert. (2)	5.2.2
C_{wmin}, C_{wmax}	BB count limits	1 pair per channel	5.3.1.a
ΔC_{wmax}	Max. BB count difference in a cal. cycle	1 per channel	5.3.1.b
C_{cmin}, C_{cmax}	SV count limits	1 per channel	5.3.2.a
ΔC_{cmax}	Max. SV count difference in a cal. cycle	1 per channel	5.3.2.b
x_w	Min. BB count smoothing weight	1	5.4.2.a
x_c	Min. SV count smoothing weight	1	5.4.3.1
glint_crit	Sun glint distance limit	1 per FOV (3)	6.4
Error est. parameters			
$\Delta Tb_{w,fixed}$	BB Tb fixed error term	1 per channel	5.1.3
ΔTb_{NL}	Diff. between quadratic and linear transfer func	1 per channel	6.3
ΔTb_{sys}	Uncertainty due to gain fluctuations	1 per channel	6.3

5. Calibration processing steps

In this section we describe how the on-board calibration measurements are used to determine the calibration coefficients, as discussed in Section 3. In summary, the procedure – illustrated in Fig. 13 – is as follows. Each channel is treated separately.

1. Determine the blackbody brightness temperature, T'_w, from its physical temperature as measured by the embedded PRT's and a possibly temperature dependent bias correction
2. Estimate the cold-space view brightness temperature, T'_c, taking into account earth radiation into the antenna sidelobes and a correction to the Rayleigh-Jeans approximation per Eq. 3-11
3. Average the blackbody and cold-space radiometer counts, C_w and C_c, measured in a calibration cycle (i.e. 4 values) and smooth the averages over several calibration cycles
4. Determine the radiometer gain, from Eq. (3-9)
5. Estimate a scene brightness temperature from the linear approximation of Eq. 3-6
6. Use the linear approximation to estimate the relative brightness temperature, x in Eq. 3-5
7. Estimate the radiometer nonlinearity amplitude, T_{NL}, in Eq. (3-4), possibly based on a measured instrument temperature
8. Compute a quadratic correction of the brightness temperature per Eq. 3-4

This implicit transfer function is applied to the earth-scene radiometer counts for one scan cycle.

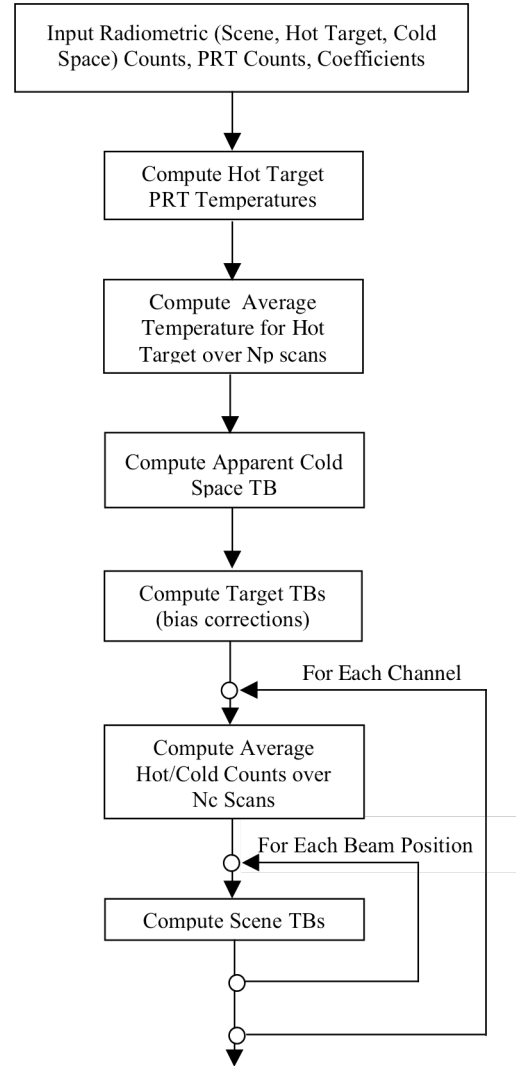Quality checking and flagging is performed and acted upon at every step.

Figure 13. Calibration flow chart

Physical temperatures

Several calibration steps require the conversion of a PRT raw count to a corresponding physical temperature. The procedure for such conversions is common to all PRTs. In essence, a PRT is a passive sensor with a resistance that is a known function of temperature. An analog-to-digital converter (ADC) outputs a digital 'count' that is proportional to the resistance, which is inserted

into the telemetry. The conversion to temperature has two steps. In the first step, the resistance is reconstructed with a linear transfer function that is calibrated with on-board measurements of a known reference resistor (the so-called precision analog monitor – PAM). This conversion is

$$R_{PRT} = R_{PAM} (C_{PRT} - C_{off})/(C_{PAM} - C_{off})$$

where C_{off} refers to a reference count with shorted inputs (i.e. zero resistance). (Thus, the essentially linear ADC is "calibrated" on-board with two reference measurements, just as is done for the slightly nonlinear radiometer.)

The second step is to convert the resistance to a temperature value. Here, the transfer function – called the Callendar-Van Dusen equation – is nonlinear:

$$R_x = R_0 \{1 + \alpha[T_x - \delta(T_x/100 - 1)(T_x/100) - \beta(T_x/100 - 1)(T_x/100)^3]\}$$

where the coefficients R_0, α, β and δ are characteristic (and determined by the manufacturer) for each individual PRT, and the temperature is in °C. This equation is solved for T_x by Newton-Raphson iteration. A simpler alternative approach, used with the AMSU systems, is to fit a cubic polynomial, $T = c_0 + c_1C + c_2C^2 + c_3C^3$, to the two functions expressed in Eq. 5-1 and Eq. 5-2, which can be done with negligible error.

Using one of these methods, all PRT readings are converted to temperatures. This is done in the L1a PGE and the results passed to the L1b PGE.

5.1 Effective Blackbody Brightness

5.1.1 Physical temperature

In summary: The warm load physical temperature is determined as the average value derived from the embedded PRT's plus a bias-like correction factor which depends on the receiver's physical temperature. Only PRT values which have passed a quality check are used. A minimum number of acceptable measurements is required — otherwise, the calibration cycle is flagged as unusable.

a. PRT conversion

One of the methods described above is used to convert all blackbody PRT readings to physical temperatures. These then undergo a series of quality checks, as follows.

b. PRT quality checking — limits

The converted warm load PRT temperatures are checked against predetermined gross limits. Those which fall outside the limits are flagged as bad:

$$T_i < T_{min} \text{ or } T_i > T_{max} \qquad \Rightarrow \qquad \text{"bad-}T_i\text{"}$$

c. PRT quality checking — self consistency

The PRT temperatures are next checked for internal consistency. This is done by comparing all temperatures not flagged as bad with each other. Any PRT's temperature that differs by more than a fixed limit from at least two other PRT readings will be flagged as bad:

$$|T_i - T_j| > \Delta T_{max1} \text{ and } |T_i - T_k| > \Delta T_{max1} \qquad \Rightarrow \text{"bad-}T_i\text{"}$$

d. PRT quality checking — data sufficiency

If the number of PRT readings not flagged as bad falls below a minimum, it is not possible to reliably determine the warm load temperature for that calibration cycle. The cycle is then flagged as uncalibrateable:

$$\sum_i w_i < N_{min} \qquad \Rightarrow \text{"bad-wcal}_L\text{"}$$

where w_i are flag-equivalent binary weights, i.e. $w_i = 0$ if "bad-T_i" is set, $w_i = 1$ otherwise. The subscript L is the current calibration cycle index.

e. PRT quality checking — cross consistency

The PRT temperatures are then checked for consistency across calibration cycles. This is done by comparing each temperature not flagged as bad with the most recent non-flagged value from the same PRT. (This is usually the value obtained in the immediately preceding calibration cycle — but not necessarily.) If the difference exceeds a maximum limit, the current PRT value is flagged as bad:

$$|T_i[\text{current}] - T_i[\text{recent}]| > \Delta T_{max2} \qquad \Rightarrow \text{"bad-}T_i\text{"}$$

Each PRT temperature which is not flagged as bad in this step is saved, to be used as the most recent accepted value in the next cycle.

[Note: The procedure described above should be re-examined and perhaps supplemented, to ensure that it does not cause rejection of good data (e.g., following a sudden recovery from a slowly evolving degradation).]

f. PRT quality checking — data sufficiency

Finally, the number of non-flagged temperatures is again checked (as in step *d* above) and the cycle is flagged as uncalibrateable if the test fails:

$$\sum_i w_i < N_{min} \qquad\qquad => \text{"bad-wcal}_L\text{"}$$

This flag is saved for use in subsequent calibration cycles.

g. Average PRT temperature

Assuming that this calibration cycle has not been flagged as bad, the average of the current non-flagged temperatures is determined:

$$<T_w> = \sum_i w_i T_i \, / \sum_i w_i$$

where each PRT temperature is weighted by the "bad-T_i"-flag equivalent weight described above. This is the best estimate of the physical temperature of the warm calibration target.

i. Blackbody temperature bias correction

A warm load temperature bias correction may be applied in two ways. The first option applies a fixed bias for each of the 5 bands (K, Ka, V, W and G). The K band covers channel 1. The Ka band covers channel 2. The V band covers channels 3-15. The W band covers channel 16. The G band covers channels 17-22. For the second option, a temperature dependent bias correction is applied for each channel, which is assumed to be of at most quadratic form

$$\Delta T'_w = a + bT_r + cT_r^2$$

where the coefficients a, b and c are also specified in the ancillary data tables (one set for each channel) and T_r is an instrument temperature that is representative of the receiver base plate. This makes it possible to allow for any slightly nonlinear temperature dependent biases that may be determined from ground testing. Extensive analysis of test data is required for this implementation (e.g., identification of temperature dependence and polynomial functional fits). For this approach, the respective receiver (RF shelf) temperatures are quality checked as in step a) and step d) above:

$$T_r < T_{low} \text{ or } T_r > T_{upp} \qquad\qquad => \qquad \text{"bad-}T_r\text{"}$$

$$|T_r[\text{current}] - T_r[\text{recent}]| > \Delta T_{rmax} \qquad\qquad => \qquad \text{"bad-}T_r\text{"}$$

If the receiver temperature is thus not flagged as bad, it is saved for use as the most recent value in the next calibration cycle. For each receiver there is both a primary and a secondary PRT. The processing step described above is performed for both. The secondary reading is used if the primary one fails.

Channels 12-15 use two redundant PLLOs, which may have different temperature dependence. The blackbody temperature bias correction algorithms allows for this possibility by using the PLLO selection state as a table selector.

j. Effective warm load temperature

The final step is to add the bias correction determined in step *i* to the physical temperature determined in step *g*:

$$T_w(ch) = <T_w> + \Delta\mathcal{T}'_w(ch)$$

The result is one value for each channel.

5.1.2 Blackbody brightness temperature

a. Effective radiometric temperature

We account for spectral nonuniformity of the calibration target by making use of a set of predetermined channel-dependent tables of coefficients to transform the target's physical temperature to an effective radiometric temperature. This effect, which accounts for deviations from the otherwise accurate monochromatic assumption, is only significant for channels which cover a relatively wide frequency range, such as the 183-GHz channels. (E.g., for channel 18 the range between the lower edge of the lower sideband and the upper edge of the upper sideband is 16 GHz, i.e. 8.7%.) A linear relationship is assumed. Thus, two coefficients are determined for each channel by lookup in the relevant table.

$$T_w'(ch) = b_0(ch) + b_1(ch)T_w(ch)$$

b. Blackbody brightness temperature

The brightness temperature is simply the radiometric temperature determined above times the emissivity, ε (which is close to 1):

$$Tb_w(ch) = \varepsilon T_w'(ch)$$

There is one value for each channel, except if the "bad-wcal" flag has been set, in which case Tb_w is undefined for all channels.

c. Blackbody radiance

An alternative physical radiance, often used by NOAA but less frequently by NASA, is determined by applying Planck's function (in wavelength space but in terms of frequencies) to T_w':

$$R_w(ch) = \varepsilon \, r \, / \, [\exp(hf/kT_w') - 1]$$

where the constant r is defined in terms of Planck's constant, h, and the speed of light, c:

$$r = 2hf^5/c^3$$

and

f	the frequency
h	Planck's constant
k	Boltzmann's constant
c	the speed of light

5.1.3 Estimated uncertainties

The uncertainty in Tb_w is computed per Eq. (3-13):

$$\Delta Tb_w(ch) = RSS\{\Delta \varepsilon T'_w(ch) \, ; \, \{\Delta \mathbf{Tb}_{w,fixed}\}_{ch}\}$$

The second term in the expression above represents a table lookup for each channel.

This expresses the uncertainty of a single measurement, estimated from a priori system uncertainties and parameters. An equivalent empirical estimate can be made by statistical analysis of the measurements.

5.2 Effective Space Brightness

5.2.1 Cosmic background temperature

A value of $T_c = 2.72$ K is used.

5.2.2 Lunar contamination

The moon may occasionally appear within the cold calibration field of view. Due to the polar orbit of the platform, it will always appear to be near the -90° phase, i.e. half-full and waxing. It will then have a brightness temperature of approximately 170-200 K (it appears warmest at the lowest frequencies). Its angular extent is about 0.5°. Lunar radiation could therefore be significant against a cold sky background, especially for the narrow-beamed ch. 17-22. Furthermore, a "lunar encounter" is likely to last for several calibration cycles, since the spacecraft advances only about 0.16° per scan cycle relative to the earth. Thus, in a worst case, the moon could appear within the half-power beamwidth for about 7 cycles, and significant contamination could last considerably longer.

We will approach this problem by comparing the moon's location relative to the cold calibration field of view with predetermined criteria of significant contamination and set a rejection flag based on the result. Thus, if significant lunar contamination is predicted, the associated cold calibration measurements are simply flagged as bad (i.e. discarded).

This step is implemented in two parts. The first part, which is done as part of the L1a processing, consists of computing the angle between the unit vectors to the center of the moon and the cold space view direction, α. (This is done using the EOSDIS Toolkit.) There are four angles for each scan mirror (i.e. for ch. 1-15 and for ch. 16-22), since the scan mirrors are not stationary during the consecutive cold calibration samples. The second part, which is done as part of the L1b processing, consists of comparing the relative lunar angle with precomputed interference limits. The test is

$$\alpha > \alpha_{max} \qquad\qquad => \text{"bad-ccal}_L\text{"}$$

If the "bad-ccal" flag has not been set we proceed with the following steps.

It should be pointed out that, since lunar 'encounters' are entirely predictable, it may be feasible to avoid the contamination problem by switching to one of the alternate space view positions during the predicted encounter. Although this will result in a discontinuity in the cold calibration time series, that may be preferable to a substantial gap in the data. The initial shakedown period after launch will permit proper characterization of the different space view positions, so that uncertainties can be minimized.

It is also possible to predict the amount and sequence of lunar contamination, i.e. compute a cold-cal correction. However, that requires very good knowledge of the socalled RF boresight pointing, which may differ from channel to channel and is initially not precisely known. It may be possible to analyze on-orbit data to determine the pointing angles to sufficient accuracy that a lunar correction scheme could be implemented. Such an algorithm has been implemented by NOAA, but we do not expect to implement it here until possibly later in the mission. The interested reader is referred to the NOAA/JPSS ATBD for details.

5.2.3 Cosmic-background brightness temperature

We use the so-called thermodynamic brightness temperature, which is defined as

$$Tb = (hf/k)\{[\exp(hf/kT) - 1]^{-1} + 0.5\}$$

This expression thus relates brightness temperature, Tb, to physical (radiometric) temperature, T. Although this transformation should strictly always be applied, in practice it is only necessary to use it when the physical temperature is very low or the frequency very high. Here it is used for the cold space view only. Thus:

$$Tb_c^0(ch) = (hf/k)\{[\exp(hf(ch)/kT_c) - 1]^{-1} + 0.5\}$$

This results in one value for each channel.

5.2.4 Sidelobe correction

To account for radiation from earth received into the antenna sidelobes during cold calibration, both direct and reflected off spacecraft surfaces, as well as radiation from the spacecraft itself, we allow for the use a 3-dimensional table relating sidelobe contribution to geographic location (latitude & longitude) and time. There is a table set for each channel, resulting in a channel-dependent sidelobe term. There is a complete set of tables for each allowed cold calibration position (see discussion in 3.2).

Initially, a single value per channel or a single value per band will be used, precomputed for each of the four possible space view positions. The somputations are based on the measured antenna patterns and a single climatologic average brightness temperature of the Earth for each channel. It is anticipated that the dimensionality and granularity of the sidelobe corrections will be increased after launch based on analysis of actual on-orbit observations. These tables will be updated from time to time. The processing is then

$$\Delta Tb_c^e(ch) = \{\mathbf{\Delta Tb}_{SL}(ch)\}_{lat,lon,time,k}$$

where k is the cold calibration position index discussed in 3.2. It is used to select the appropriate set of tables. This results in one value for each channel. However, as mentioned above, the table dimensionality is greatly reduced in the initial implementation.

5.2.5 Effective space brightness temperature and radiance

The total estimated space-view brightness temperature (and the corresponding physical radiance) can now be determined:

$$Tb_c(ch) = Tb_c^0(ch) + \Delta Tb_c^e(ch)$$

and

$$R_c(ch) = r\,[kTb_c(ch)/hf(ch) - 0.5]$$

There is one value for each channel, except if the "bad-ccal" flag has been set, in which case Tb_c is undefined for all channels.

5.2.6 Estimated uncertainties

The uncertainty in Tb_c is computed per Eq. (3-13):

$$\Delta Tb_c^{rms}(ch) = \{\Delta \mathbf{Tb}_{SL}(ch)\}_{lat,lon,time}$$

The right-hand side represents a table lookup identical to that of 5.1.3.

5.3 Radiometric Calibration Counts

Each of the two calibration targets (i.e. the warm load and cold space) is sampled four times in rapid succession. The results are digital "counts" which represent the radiometer's output. It is assumed that the radiative environment does not change between successive samplings, so that any differences between the measurements are strictly due to noise — which can be reduced by averaging the measurements.

The procedure described below is identical for both targets. A software implementation would naturally take advantage of that and simply use parameter tables to account for numerical differences, as discussed previously.

5.3.1 Warm load counts

a. Quality check — limits

Each count from each channel is checked against channel-specific gross limits. Those which fall outside the limits are flagged as bad:

$$C_{wi}(ch) < C_{wmin}(ch) \ \text{ or } C_{wi}(ch) > C_{wmax}(ch) => \text{"bad-w}C_i(ch)\text{"}$$

Initial values for the gross limits are supplied by NGES. They may be updated based on operational experience, especially during the initial shakedown period after launch.

b. Quality check — self consistency

The counts are next checked for internal consistency. This is done by checking the measurement spread against a channel-specific limit. (An appropriate set of values for these limits will be determined during the initial shakedown period after launch.) The calibration cycle is flagged as bad for any channel which fails this test:

$$MAX[\{C_w(ch)\}] - MIN[\{C_w(ch)\}] > \Delta C_{wmax}(ch) => \text{"bad-w}C_L(ch)\text{"}$$

where L is the current calibration cycle index.

c. Average counts

We now compute, for each channel, the average calibration count for the current cycle. Thus, for each channel which has not been flagged as "bad-wC_L" in step *b*, we compute the average of the counts which have not been flagged as "bad-wC_i" in step *a*:

$$C_{wavgL}(ch) = \sum_i w_i(ch)C_{wi}(ch) / \sum_i w_i(ch)$$

where $w_i(ch)$ is a particular channel's flag-equivalent binary weight (from step *a*) for sample i (i =1..4), as described in 5.1.1.*d*. This results in one value for each channel, except for those channels which have been flagged as "badwC_L", which are undefined.

<u>5.3.2 Cold space counts</u>

a. Quality check — limits

Each count from each channel is checked against channel-specific gross limits. Those which fall outside the limits are flagged as bad:

$$C_{ci}(ch) < C_{cmin}(ch) \text{ or } C_{ci}(ch) > C_{cmax}(ch) => \text{"bad-}cC_i(ch)\text{"}$$

b. Quality check — self consistency

The counts are next checked for internal consistency. This is done by checking the measurement spread against a channel-specific limit. (An appropriate set of values for these limits will be determined during the initial shakedown period after launch.) The calibration cycle is flagged as bad for any channel which fails this test:

$$\text{MAX}[\{C_c(ch)\}] - \text{MIN}[\{C_c(ch)\}] > \Delta C_{cmax}(ch) => \text{"bad-}cC_L(ch)\text{"}$$

where L is the current calibration cycle index.

c. Average counts

We now compute, for each channel, the average calibration count for the current cycle. Thus, for each channel which has not been flagged as "bad-cC_L" in step b, we compute the average of the counts which have not been flagged as "bad-cC_i" in step a:

$$C_{cavgL}(ch) = \sum_i w_i(ch)C_{ci}(ch) / \sum_i w_i(ch)$$

where $w_i(ch)$ is a particular channel's flag-equivalent binary weight (from step a) for sample i (i = 1..4), as described in 5.1.1.d. This results in one value for each channel, except for those channels which have been flagged as "badcC_L", which are undefined.

5.4 Smoothed Calibration Counts

In order to attain accurate and stable calibration it is desirable to reduce the random noise in the calibration counts before determining the calibration coefficients. This is done by averaging or smoothing over several calibration cycles bracketing the cycle that is being calibrated. Typically, a weighting function that is centered on the current cycle, is symmetric and declines toward the ends of a specified range. For AMSU, a linear function spanning ±3 cycles is used, where the weights are 1.00 at the center, 0.75 at ±1, 0.50 at ±2, and 0.25 at ±3, and the weighted sum is scaled by 4. This is illustrated in Figure 14.
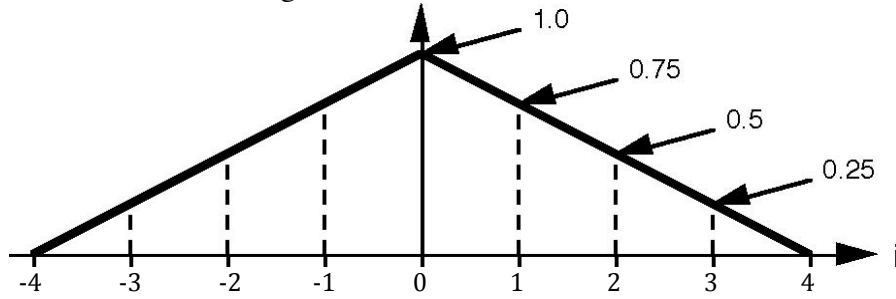

Figure 14: Smoothing function — example for 7-point smoothing (n = 3)

We assume that the preceding steps have been carried forward at least n cycles beyond the current calibration cycle and that the results from the preceding n cycles are accessible..

5.4.1 Smoothing function

The possible smoothing range is limited at the low end by the need to reduce the effective noise and at the high end by 1/f noise (correlated instrument noise), and there is an optimal range that minimizes the effective noise. Several ATMS cannels are exhibiting pronounced 1/f noise, and ways to ameliorate this are under active investigation. Here we will simply assume that the smoothing parameters are provided in processing tables, including the shape of the smoothing function. This allows for an arbitrary smoothing function with channel-dependent range. We denote it by W_i, where $i = -n \ldots +n$.

5.4.2 Smoothed warm load counts

For each channel we compute the weighted average of those cycle averages which have not been flagged as "bad-wC_L" in step 5.3.1.*b*. Again we use flag-equivalent binary weights, w, to account for the flag conditions (i.e. $w_L = 0$ if "bad-wC_L" is set and $w_L = 1$ otherwise).

a. Data sufficiency check

We first check if there is enough valid data available to compute a meaningful weighted average. We now require that the sum of the smoothing weights for the available data does not fall below a minimum fraction of the total possible:

$$\sum_i W_i w_{L+i}(ch) / \sum_i W_i < x_w \qquad\qquad => \text{"bad-wcal}_L(ch)\text{"}$$

where i = -n .. +n, x_w is the minimum-weight fraction mentioned above, and $w_{L+i}(ch)$ is the "bad-wC"-flag equivalent weight for the calibration cycle which is offset by i cycles from the current (L) cycle.

b. Weighted average counts

For all channels which passed the test in step *a*, we can now compute a weighted average:

$$\langle C_w(ch)\rangle = \sum_i W_i w_{L+i}(ch) C_{wavg,L+i}(ch) / \sum_i W_i w_{L+i}(ch)$$

where $C_{wavg,L+i}$ is the average warm count for cycle L+i earlier determined in step 5.3.1.c. There is one value for each channel, except for those channels with the "bad-wcal$_L$" flag set, which are undefined.

5.4.3 Smoothed cold space counts

For each channel we compute the weighted average of those cycle averages which have not been flagged as "bad-cC$_L$" in step 5.3.2.*b*. Again we use flag-equivalent binary weights, w, to account for the flag conditions (i.e. $w_L = 0$ if "bad-cC$_L$" is set and $w_L = 1$ otherwise).

a. Data sufficiency check

We first check if there is enough valid data available to compute a meaningful weighted average. We note that the sum of the smoothing weights is n+1 (i.e. if the data from both the current, the n preceding and the n succeeding cycles were available, the total data weight would be n+1). We now require that the sum of the smoothing weights for the available data does not fall below a minimum fraction of the total possible:

$$\sum_i W_i w_{L+i}(ch) / \sum_i W_i \; < x_c \qquad\qquad \Rightarrow \text{"bad-ccal}_L(ch)\text{"}$$

where i = -n .. +n, x_c is the minimum-weight fraction mentioned above, and $w_{L+i}(ch)$ is the "bad-cC"-flag equivalent weight for the calibration cycle which is offset by i cycles from the current (L) cycle.

b. Weighted average counts

For all channels which passed the test in step *a*, we can now compute a weighted average:

$$\langle C_c(ch)\rangle = \sum_i W_i w_{L+i}(ch) C_{cavg,L+i}(ch) / \sum_i W_i w_{L+i}(ch)$$

where $C_{cavg,L+i}$ is the average cold count for cycle L+i earlier determined in step 5.3.2.*c*. There is one value for each channel, except for those channels with the "bad-ccal$_L$" flag set, which are undefined.

5.5 Calibration Coefficients

For each channel we will now determine three coefficients, defined in Eqs. (3-7), (3-8), and (3-9) which define the quadratic relationship between brightness temperature and radiometer count described in Eq. (3-3).

5.5.1 Calibration quality flag check

The first step is to check if there is sufficient calibration data to determine a new set of calibration coefficients. If that is not the case, we will use the most recent set of coefficients instead. We proceed as follows:

a. Undefined brightness temperatures — all channels

      "bad-wcal$_L$" or "bad-ccal$_L$"   => "bad-cal(ch)" for all channels

where the flags originate from 5.1.1 and 5.2.2, respectively.

b. Undefined calibration counts — single channels

      "bad-wcal$_L$(ch)" or "bad-ccal$_L$(ch)"   => "bad-cal(ch)" for that channel

where the flags originate from 5.4.2 and 5.4.3, respectively.

5.5.2 Nonlinear term

This step may be skipped if the "bad-cal" flag is set for all channels, as in *a* above. We will assume that the nonlinearity is purely a function of the instrument temperature and that the form of that function remains as it was characterized during pre-launch testing. We use the same instrument temperature that was used in 5.1.1.i to determine the warm load temperature correction factor, T_r. Here, as in that case, we also have a set of table pairs determined from pre-launch test data. The first table component is a list of receiver temperatures and the second component is a list of nonlinearity terms — as defined in Eqs. (3-4) and (3-6) in Section 3 — observed at those temperatures. There is a table pair for each channel. The object of this step is to interpolate these tables at the receiver temperature determined earlier. The nonlinear term is then:

      u(ch) = *interpolate* [{$\mathbf{T_r}$, $\mathbf{u}$(ch)}] *at* T_r

There is one value for each channel.

5.5.3 Gain

This step is always skipped if the "bad-cal" flag is set for all channels, as in 5.5.1.*a* above. We determine the gain for each channel according to the following formula, for all channels which do not have the "bad-cal" flag set:

      g(ch) = [<C_w(ch)> - <C_c(ch)>] / [Tb_w(ch) - Tb_c(ch)]

where

$<C_w(ch)>$ is the smoothed warm load count, from 5.4.2
$<C_c(ch)>$ is the smoothed cold space count, from 5.4.3
$Tb_w(ch)$ is the estimated warm load brightness temperature, from 5.1.2
$Tb_c(ch)$ is the estimated cold space brightness temperature, from 5.2.5

5.5.4 Calibration coefficients

a. Good calibration data

For each channel which does not have the "bad-cal" flag (from 5.5.1) set we compute the coefficients as follows (cf. Eqs. (3-7), (3-8) and (3-9)):

$$a_2(ch) = u(ch) / g^2(ch)$$

$$a_1(ch) = 1/g(ch) - a_2(ch) [<C_w(ch)> + <C_c(ch)>]$$

$$a_0(ch) = Tb_w(ch) - <C_w(ch)>/g(ch) + a_2(ch) <C_w(ch)> <C_c(ch)>$$

These values are saved as the most recent coefficients for each channel processed.

b. Bad calibration data

For each channel which has the "bad-cal" flag set we use the most recent coefficients:

$$a_i (ch) = a_i(ch)[recent] \text{ for } i = 0 .. 2.$$

6. Computation of Brightness Temperatures

In this section we *apply* the calibration coefficients determined in Section 5 to all earth scene measurements in a scan cycle (i.e. in a scan line). The results are conventionally called antenna temperatures. We will not apply a correction to reduce the effect of far sidelobe spillover into cold space near the swath edges – often called the scan bias. The results after such a correction are conventionally called brightness temperatures. This scan bias effect does not reflect a calibration issue but is rather a scene effect. It is therefore more properly dealt with in L2 or in an L2 preprocessor. (NOAA/JPSS implements this in a TDR to SDR step, which may be viewed as such a preprocessor.) We will also not implement spatial resampling of ATMS antenna temperatures to CrIS FOV locations, which NOAA also implements in the TDR to SDR step, since such remapping is properly part of L2 processing (possibly implemented as a preprocessor).

6.1 Radiometric Calibration

We assume that the calibration coefficients change slowly compared with a scan cycle, so that the coefficients derived from a particular cycle can be applied to all radiometer measurements in that cycle — even though there may be a time lag of up to 2 seconds between scene measurements and the corresponding calibration measurements. (This assumption will be re-examined after launch.)

Then, for each channel (ch) and each scan position (i), the antenna temperatures are, as defined by Eq. (3-3):

$$Ta(ch,i) = a_0(ch) + a_1(ch)\,C(ch,i) + a_2(ch)\,C^2(ch,i)$$

where the a's are the calibration coefficients determined in Section 5 for the current scan cycle and the C's are the radiometer counts.

6.2   Estimated Radiometric Sensitivity

We will provide a simple but rough empirical estimate of the radiometric accuracy (or, more correctly, precision or sensitivity), NEDT, by computing the standard deviation of the four consecutive blackbody counts and dividing by the gain to convert to temperature.

$$NEDT \approx STD(C_{w,1..4})/g$$

where STD is the standard deviation. The same quality flag checking as in 5.3.2 should be applied. Better estimates can be obtained by aggregating the NEDT values from individual scans over a longer time period.

6.3   Estimated Calibration Accuracy

We determine the calibration accuracy for each channel per Eq. (3-13). Substituting brightness temperatures, we get

$$\Delta Tb_{cal}(ch,i) = \{[x\, \Delta Tb_w]^2 + [(1-x)\, \Delta Tb_c]^2 + [4(x-x^2)\, \Delta Tb_{NL}]^2 + [\Delta Tb_{sys}]^2\}^{1/2}$$

where

$x = (Ta(ch,i) - Tb_c)/(Tb_w - Tb_c)$

$\Delta Tb_w = \Delta Tb_w{}^{rms}(ch)$

$\Delta Tb_c = \Delta Tb_c{}^{rms}(ch)$

$\Delta Tb_{NL} = \{\Delta Tb_{NL}(ch)\}_{ch}$

$\Delta Tb_{sys} = \{\Delta Tb_{sys}(ch)\}_{ch}$

This results in one value per channel for each earth scene. Note that this, unlike the estimate discussed in 5.4, is not an empirical estimate of precision but rather represents an expectation value of absolute accuracy based on known instrument characteristics and the radiometric environment. Also, the procedure described in 5.4 yields one channel set per scan line, while the procedure described here yields one channel set per footprint.

6.4   Sun glint

The following section is provided as an aid to users. The effect discussed does not involve calibration issues but is covered here because it depends on geolocation that is easily available in the L1a and L1b files.

The Earth's surface can be quite reflective (ocean reflectivity can exceed 0.5 at some microwave frequencies), as well as scattering. Therefore, there will be both specularly reflected and scattered solar radiation coming from the surface. Since the brightness temperature of the sun is on the order of 10,000 K, this can result in substantial microwave radiation at viewing angles close to the direction of specular reflection.

Whether this becomes a problem depends on the orbit. The design orbit for NPP is a sun synchronous orbit with a 1:30 PM ascending node and an inclination of about 98°. Thus, the sun's longitude at the spacecraft's northbound equator crossing is 22.5° west of the subsatellite point (nadir). At the equator, the microwave instruments scan out to about 8° west of the nadir point (a 49° nadir angle from a 825-km altitude) and about 1° south (due to the inclination of the orbit). Within the scan swath the solar angle of incidence will increase from about 14.3° (at the swath edge) to 22.3° (at nadir). On the other hand, the instrument's viewing angle of incidence increases from 0° (at nadir) to 57° (at the swath edge). Somewhere within the western half of the swath there must therefore be a point where the two angles of incidence are equal and specular reflection results. For the NPP orbit this will happen at approximately 3° west of nadir, or at a nadir scan angle of approximately 17°, where the angle of incidence is about 20°. (These angles are only approximate and will change with the season.) It is certain, however, that specular reflection conditions will exist once per orbital revolution (namely, approximately 3° north of the crossing of the plane of the ecliptic).

The relevant surface properties are very variable and unpredictable. We will therefore approach this problem in a purely geometric sense, by computing a sun glint "proximity index" for each scan position. This index, which is proportional to the inverse of the distance between a footprint and the sun glint spot, will be a measure of the likelihood of sun glint effects. The user must apply surface information and must be aware of the masking effect of high atmospheric opacity. (It is only relatively transparent channels that might be affected by sun glint.)

The EOS Toolkit is used to determine the location of the sun glint for each scan position. Its

distance from the center of the footprint on the surface is then computed, and finally the ratio between a predetermined scale length and the sun glint distance is truncated to an integer valued sun glint index. If the index has a high value, indicating a high likelihood of sun glint contamination of surface channels, a flag is set. Thus, the steps are, for each footprint

1. Compute latitude and longitude of the sun glint spot (if any)
2. Compute the distance between footprint center and the sun glint spot, d_glint
3. Compute glint_index = L_glint/d_glint
4. Set the flag: If glint_index > glint_crit   => "possible glint"

L_glint and glint_crit are predetermined parameters, which may be updated later.

It is expected that this algorithm, as well as the parameters, will be updated subsequent to launch, based on analysis of on-orbit observations.

6.5   Coast Contamination

The following section is also provided as an aid to users. The effect discussed does not involve calibration issues but is covered here because it depends on geolocation that is easily available in the L1a and L1b PGEs.

While the ATMS "beam width" ranges from 1.1° to 5.2°, a significant fraction of the radiation received comes from outside this 3-dB beam. About 95-99% of the energy comes from the so-called main beam, which is defined as 2.5x the beam width. The effect of this is to smear out sharp edges in the observed field. This is particularly the case at coastlines, where the emissivity may sudenly change by more than 0.5 in some channels. Thus, the brightness temperature might be 150 K over the ocean and jump to 300 K over land. The wide and "fuzzy" beam will smear out the resulting 150 K step and make it noticeable far away from the coast itself. Unless accounted for, this can result in large errors.

The purpose of the coast contamination algorithm is twofold: to indicate to the user that there is likely coastal contamination in some channels, and to provide a quantitative estimate of its magnitude which can be used in downstream (L2) corrective processing. The intention is to provide a "beam weighted" land/ocean fraction (called 'landfrac') which will indicate how much of the received radiation originates from an ocean surface (vs. land) to a sufficient accuracy that it can be used in the retrieval processing to compensate for the blurring effect without unduly amplifying the effective measurement noise. A user flag will be derived from this fraction. Without the ability to compensate for such contamination, a measurement thus flagged would have to be rejected from further processing.

6.6   Quality Assessment

A number of flags and other indicators will be used to alert the user to potential problems and in general indicate the estimated quality of the calibration process and its results. This will not be discussed in detail here, but we will provide a summary. Quality Assessment parameters are provided at several data granularities: at the swath file level (the "granule" in EOS nomenclature — in the current design this consists of 180 ATMS scan lines), at the scan line level (i.e. per calibration cycle), and at the footprint level. Most of the quality assessment is generated at the

scan line level and presented to the user along with the primary data parameters per scan line. Most of these parameters are then summarized at the "granule" level. Some of them are further summarized on a daily basis in a browse product.

The QA parameters fall into the following categories

- Quality of the input data per L1a processing QA
- Quality of the input data per L1b data testing
- Quality of the calibration processing steps
- Error estimates
- Problem indicators not related to calibration processing

In addition to such QA parameters, every data product (e.g., calibrated brightness temperatures) will have error estimates associated with it. The algorithms discussed in preceding sections include descriptions of how such error estimates are derived.